

A class of enhanced physics-informed neural networks for data-driven solitons and parameters discovery to (2+1)-dimensional coupled nonlinear Schrödinger systems with variable coefficients: vector dark and anti-dark one- and two-solitons

Hamid Momeni<sup>1</sup>

<sup>1</sup>Independent Researcher.

Contributing authors: [momeni.umz@gmail.com](mailto:momeni.umz@gmail.com);

**Abstract**

This paper investigates data-driven solutions and parameter discovery to (2+ 1)-dimensional coupled nonlinear Schrödinger equations with variable coefficients (VC-CNLSEs), which describe transverse effects in optical fiber systems under perturbed dispersion and nonlinearity. By setting different forms of perturbation coefficients, we aim to recover the dark and anti-dark one- and two-soliton structures by employing an enhanced physics-based deep neural network algorithm, namely a physics-informed neural network (PINN). The enhanced PINN algorithm leverages the locally adaptive activation function mechanism to improve convergence speed and accuracy. In the lack of data acquisition, the PINN algorithms will enhance the capability of the neural networks by incorporating physical information into the training phase. We demonstrate that applying PINN algorithms to (2+ 1)-dimensional VC-CNLSEs requires distinct distributions of physical information. To address this, we propose a region-specific weighted loss function with the help of residual-based adaptive refinement strategy. In the meantime, we perform data-driven parameter discovery for the model equation, classified into two categories: constant coefficient discovery and variable coefficient discovery. For the former, we aim to predict the cross-phase modulation constant coefficient under varying noise intensities using enhanced PINN with a single neural network. For the latter, we employ a dual-network strategy to predict the dynamic behavior of the dispersion and non-linearity perturbation functions. Our study demonstrates that the proposed framework holds significant potential for studying high-dimensional and complex solitonic dynamics in optical fiber systems.

**Keywords:** Physics-informed neural networks, Dual-network, (2+ 1)-dimensional coupled non-linear Schrödinger equations, Data-driven solitons, Parameter discovery

## 1 Introduction

In the field of optical fiber communication, nonlinear differential equations are commonly used to model the behavior of light propagation through the fiber. These equations take into account factors such as dispersion, nonlinearity, and attenuation to accurately predict the signal transmission in optical fibers. Nonlinear differential equations are essential for understanding the complex interactions between light and the fiber medium, allowing researchers to optimize signal transmission and minimize data loss. By incorporating these factors into mathematical models, engineers can design more efficient and reliable optical communication systems [1–14]. One of the most important equations used in this context is the nonlinear Schrödinger equation (NLSE). The NLSE is a fundamental partial differential equation that describes the evolution of the slowly varying envelope of a pulse of light in an optical fiber, considering the effects of both dispersion and nonlinearity. Specifically, it captures the balance between the dispersive effects, which tend to spread the pulse in time, and the nonlinear effects, such as self-phase modulation, which can lead to pulse shaping or even soliton formation, where the pulse maintains its shape over long distances. The NLSE and its extensions have been widely studied in many scientific disciplines, including nonlinear optics [15–17], fluid dynamics [18], quantum mechanics [19, 20], and plasma physics [21, 22]. By solving the NLSE, researchers can predict and manipulate the behavior of light pulses in optical fibers, enabling advancements in telecommunications and optical signal processing. The standard NLSE can be formulated as

$$i\psi_t + \alpha\psi_{xx} + \beta|\psi|^2\psi = 0,$$

where  $\psi = \psi(x, t)$  represents a complex amplitude of two variables  $x$  and  $t$ ,  $\alpha$  and  $\beta$  are real constants, which affect the waveform broadening and the oscillation during light wave transmission, respectively.  $i$  denotes the imaginary units and the subscript  $x$  ( $t$ ) represents the partial derivative with respect to  $x$  ( $t$ ). The second term  $\psi_{xx}$  represents the group velocity dispersion, while the third term denotes the nonlinearity. In the past few years, many numerical methods have been developed to study the dynamic behavior of NLSE, such as inverse scattering transform, Hirota method, Sardar sub-equation technique, and so on [23–30]. Many extensions to standard NLSE have been introduced to model various physical phenomena for a more accurate representation of complex systems. As one of the most effective integrable models, derivative NLSE is studied in the field of plasma physics to model Alfvén waves propagation [31, 32]. The perturbed NLSE describes the pulse propagation of high-order dispersion in an optical fiber, when realistic fibers are considered [33]. An integrable nonlocal NLSE has been introduced in [34], which is parity-time(PT)-symmetric. When considering the propagation of waveforms through multiple fields at different polarizations and

frequencies, the coupled NLSE (CNLSE) can be formulated as [35–37]

$$\begin{aligned}i\psi_{1,t} + \psi_{1,xx} + \beta(|\psi_1|^2 + \tau|\psi_2|^2)\psi_1 &= 0, \\i\psi_{2,t} + \psi_{2,xx} + \beta(\tau|\psi_1|^2 + |\psi_2|^2)\psi_2 &= 0,\end{aligned}\tag{1}$$

where  $\psi_1 = \psi_1(x, t)$  and  $\psi_2 = \psi_2(x, t)$  are the amplitudes of wave propagation through a two-mode optical fiber, the value of the parameter  $\beta = \pm 1$  is used to differentiate between the self-focusing and self-defocusing Kerr nonlinearity and the range of the parameter  $\tau$  varies,  $\tau > 2/3$  and  $\tau < 7$ , regarding the Kerr-shape electron nonlinearity and the nonlinearity resulting from molecular orientation changes [38, 39]. In [40], general  $N$ -dark-dark solitons for system (1) are obtained by applying the KP-hierarchy reduction method. Localized wave solutions including dark-dark and bright-dark solitons, breather-breather solutions, and different types of new vector rogue wave solutions as well as their interactions are studied for defocusing version of system (1) through the application of the Darboux transformations [41]. By virtue of the Hirota method, a variety of optical solitons are obtained for high-dimensional generalized CNLSE in the field of optical fiber communication [42–44].

In the field of optical fiber communication, studying the dynamic behavior of optical solitons is crucial for understanding pulse propagation, enhancing data transmission rates, and mitigating signal degradation over long distances. In the past decades, many formations of solitons have been observed in different optical fiber systems, including bright solitons, dark solitons, vector solitons, and so on. The reason for obtaining different formations of optical solitons for NLSE lies in the varying balance between dispersion and nonlinearity within the optical medium, as well as the initial conditions and parameters such as pulse shape, power, and wavelength. These different types of solitons exhibit unique properties that can be harnessed for various applications in optical communication systems [45–47]. The optical soliton solutions can maintain the shape and speed of optical pulses over long distances, effectively countering the effects of dispersion and nonlinearity in the fiber, and thus enabling high-performance and reliable data transmission.

While lower-dimensional versions of CNLSE describe the evolution of wave packets in a single spatial direction, higher-dimensional CNLS equations can model more complex physical phenomena in higher-dimensional scenarios with a broader range of behaviors and applications. Due to the presence of additional spatial variables, it is possible to model wave propagation in larger spaces rather than along a single line. The higher-dimensional CNLSE is particularly relevant for understanding phenomena like the formation and interaction of vortex solitons, two-dimensional localized structures, and pattern formation in nonlinear media. In contrast, the  $(1+1)$ -dimensional CNLSE is limited to simpler solitary wave solutions, such as bright and dark solitons, that are confined to one spatial direction. Due to the complexity of modeling with higher-dimensional versions, advanced numerical techniques and approximations are required for analysis. The  $(2+1)$ -dimensional CNLSE can be constructed as

$$\begin{aligned}i\psi_{1,t} + \psi_{1,xx} + \psi_{1,yy} + \beta(|\psi_1|^2 + \tau|\psi_2|^2)\psi_1 &= 0, \\i\psi_{2,t} + \psi_{2,xx} + \psi_{2,yy} + \beta(\tau|\psi_1|^2 + |\psi_2|^2)\psi_2 &= 0,\end{aligned}\tag{2}$$

where  $\psi_1 = \psi_1(x, y, t)$  and  $\psi_2 = \psi_2(x, y, t)$  describe the amplitudes of two circularly polarized waves. The solitonic structures of system (2) and its extensions have been discovered using a variety of numerical techniques [48–52]. In optical fiber communication, many mathematical models have been studied the evolution of complex wave envelopes in homogeneous media, where the related parameters remain fixed throughout the medium. However, many real-world systems exhibit spatial or temporal variations in their nature, such as inhomogeneous plasmas and varying refractive indices. To address these variations, the variable coefficient NLSE is introduced, where the coefficients related to dispersion and nonlinearity are allowed to vary with respect to spatial and/or temporal variables [53–56]. Considering the local defects and damages in the optical fibers, the variable coefficient (2+ 1)-dimensional CNLSE (VC-CNLSE) with perturbed dispersion and nonlinearity can be constructed as

$$\begin{aligned} i\psi_{1,t} + \alpha(t)(\psi_{1,xx} + \psi_{1,yy}) + \beta(t)(|\psi_1|^2 + \tau|\psi_2|^2)\psi_1 &= 0, \\ i\psi_{2,t} + \alpha(t)(\psi_{2,xx} + \psi_{2,yy}) + \beta(t)(\tau|\psi_1|^2 + |\psi_2|^2)\psi_2 &= 0. \end{aligned} \quad (3)$$

By choosing different forms of perturbation functions  $\alpha(t)$  and  $\beta(t)$ , one can obtain various optical solitons by controlling factors such as intensities, velocities, and accelerations. By virtue of the Hirota method, linear, parabolic, and quasi-periodic dark solitons are discovered in [57]. Abundant dark and anti-dark soliton structures, as well as their collisions are studied in [58] using the Hirota method. By utilizing the developed Hirota bilinear method, one-soliton, two-soliton, three-soliton, and breather like bright-dark solitons are observed in [59].

In the era that data analysis has become increasingly important, machine learning algorithms have emerged as powerful tools for extracting insights and making predictions from large datasets. These algorithms can automatically learn and improve from experience without being explicitly programmed, allowing for more efficient and accurate analysis of complex data patterns. Machine learning algorithms have been applied in many scientific disciplines, including natural language processing [60], image recognition [61], bioinformatics [62, 63], and climate modeling [64]. These diverse applications underscore the versatility of machine learning as a tool for solving complex data-driven problems across various domains. Deep learning is a machine learning technique that uses the universal approximation capability of neural networks to extract and learn hidden patterns within available data. These neural networks, composed of multiple layers of interconnected nodes, allow deep learning models to automatically identify and represent complex features in data. The success of deep learning can be attributed to its ability to process vast amounts of data and uncover intricate relationships that may not be apparent through traditional methods [65, 66]. By leveraging large datasets, advanced architectures, and powerful computational resources, deep learning has revolutionized numerous fields. The performance and accuracy of deep learning models are directly related to the amount of available data to be analyzed. In the lack of sufficient data acquisition, machine learning algorithms face challenges that can lead to poor performance and robustness, with no guarantee of convergence. In these scenarios, using the prior knowledge of the problem at hand in the modeling process can lead the solution space into the admissible one. This prior information can be

represented through various forms, such as domain-specific constraints, expert knowledge, or physics-based models. This approach is particularly useful in fields where data acquisition is expensive to obtain, ensuring that the model remains reliable and effective. Recently, we have witnessed the successful application of deep learning methods in the field of solving differential equations, leading to the formation of a new branch of studies, namely scientific machine learning.

As a physics-based methodology, physics-informed neural networks (PINNs) have been effectively applied in various scientific scenarios such as fluid dynamics, material science, and medical imaging. PINNs combine the power of neural networks with the physical principles governing a system to accurately predict outcomes and simulate complex phenomena [67]. In contrast to traditional numerical methods, PINNs enhance the approximation capability of deep neural networks by incorporating physical laws, described by differential equations, into the training phase. These physical laws can act as a regularization to constraint the solution space of neural networks. Training these neural networks involves solving a minimization problem, where a multi-objective loss function – combining physics-informed and data-driven losses – is optimized. This approach results in accurate predictions while ensuring consistency with the underlying physical principles. By considering the spatial and/or temporal coordinates as input data, PINNs leverage the Automatic Differentiation (AD) technique [68], enabling the efficient computation of derivatives with respect to the input variables, which are necessary to enforce the governing physical laws. Then, a multi-objective loss function can be constructed using the residual forms of the boundary and/or initial conditions, as well as the residuals related to the differential equations. This loss function is optimized during training, allowing the neural network to approximate solutions that not only fit the data but also adhere to the underlying physical principles. As a result, PINNs are able to provide accurate and physically consistent solutions even in cases where traditional methods may struggle, particularly when data is scarce or noisy [69]. While PINNs offer innovative approaches and flexibility, there are many challenges and limitations that need to be addressed [70, 71]. Some of the advantages of PINNs methodologies are that they are capable of handling problems with irregular geometries and boundary conditions, highly flexible in dealing with non-linear problems, and able to solve inverse problems where traditional methods may struggle. Additionally, they are easy to code, with no significant differences between the coding for forward and inverse problem solving.

In recent years, numerous studies have been reported on the applications of PINNs in the field of optical fiber communication. In [72], an adaptive residual points PINN scheme is introduced for vector soliton simulation and parameter discovery of general CNLSE. Data-driven vector soliton solutions and parameter discovery for the coupled mixed derivative NLSE are studied in [73], where a PINN method with a twin subnet strategy is used. In [74], an improved PINN algorithm is introduced to simulate both vector degenerate and nondegenerate solitons of the coupled nonlocal NLSE and to estimate the associated equation parameters under varying noise intensities. A PINN scheme with a locally adaptive activation function is employed in [75] for data-driven localized wave solutions of the derivative NLSE. In [76], the standard

PINNs is used for prediction of soliton dynamics and estimation of model parameters for  $(2+1)$ -dimensional NLSE. In [77], the authors employed an improved PINN algorithm for solving forward and inverse problems, where the model equation was the Hirota equation with variable coefficients. They applied the proposed algorithm for data-driven discovery of the constant coefficients and the linear function variable coefficients in the model equation.

Most of the studies mentioned above have focused on simulating the propagation of waveforms, modeled by the NLSE and its extensions, in a homogeneous environment. Traditional numerical methods face challenges in simulating high-dimensional problems due to the curse of dimensionality, which causes an exponential increase in computational cost and complexity as the number of dimensions grows. When dealing with strongly nonlinear problems, these methods may encounter difficulties such as convergence issues and numerical instability. This is particularly problematic when the coupled equations involve interactions across multiple scales or when the solution exhibits sharp gradients or localized structures like solitons. These limitations have driven the development of alternative approaches, such as PINNs, to address the shortcomings of traditional methods in modern applications. In this paper, an enhanced PINN methodology is introduced for the prediction of soliton structures to  $(2+1)$ -dimensional CNLSE (3). To the best of our knowledge, the application of PINNs to this class of equations has not been reported before. The proposed approach leverages a neuron-wise locally adaptive activation function to accelerate the convergence rate and improve the accuracy of standard PINN [78]. By combining the proposed approach with the residual-based adaptive refinement strategy (RAR) [79], we demonstrate that each residual loss constructed from the model Eq. (3) requires a different distribution of residual points within the computational domain. The performance and efficiency of the proposed framework will be evaluated in predicting various soliton dynamics through the lens of  $L^2$  relative error. By considering different forms of dispersion and nonlinearity coefficients, vector parabolic dark one-soliton, vector m-shaped anti-dark one-soliton, and dark two-soliton are predicted. We also apply the proposed framework to the parameter discovery of the model Eq. (3). First, we apply the introduced PINN, equipped with a single neural network, for constant parameter discovery under different noise intensities. This PINN model not only predicts the solution of the model equation but also estimates the constant parameter as another trainable network parameter during training. Second, we employ a dual-network strategy for the proposed PINN scheme, where one neural network predicts the solution dynamics, while the other captures the behavior of the dispersion and nonlinearity variable coefficients. The obtained results indicate that the proposed framework is promising for exploring waveform propagation in the optical fiber communications landscape.

This is how the remainder of the paper is organized. In Sect. 2, we introduce the general framework of PINN algorithms for the general  $(2+1)$ -dimensional variable coefficient coupled nonlinear equations and discuss the related mechanisms. We also introduce our enhanced PINN framework in this section. We investigate the application of the proposed enhanced PINN algorithm for data-driven vector dark and anti-dark one- and two-soliton solutions to the  $(2+1)$ -dimensional VC-CNLSE. We illustratively show that our proposed algorithm accurately captures the solitonic dynamics. We also

perform data-driven parameter discovery for the system of model equations to estimate the value of constant coefficient as well as the variable dispersion and nonlinearity coefficients. A conclusion is made in Sec. 4, where we summarize the effectiveness of the enhanced PINN framework and discuss its potential.

## 2 PINNs for the (2+ 1)-dimensional VC-CNLSE

The PINNs methodology leverages the approximation capability of deep neural networks to solve differential equations through a minimization problem. A feed-forward neural network with an appropriate architecture (in terms of depth and width) is trained to satisfy both the governing equations and the boundary and/or initial conditions by minimizing a loss function that combines physics-based residuals and data-driven errors. This approach allows the network to learn complex relationships within the data, ensuring that the solution adheres to the underlying physical laws while also capturing any observed patterns in the data. In this section, we first introduce the general framework for PINNs methods applied to the (2+ 1)-dimensional coupled nonlinear equations with variable coefficients. Next, we introduce an enhanced PINN scheme and investigate the related modifications to the standard PINNs. In doing so, we consider the general (2+ 1)-dimensional variable coefficient coupled nonlinear equation in a complex environment space as follows:

$$i\psi_{j,t} + \mathcal{N}[\psi_j, \psi_{j,\mathbf{X}}, \psi_{j,\mathbf{X}\mathbf{X}}, \dots; \lambda] = 0, \quad \mathbf{X} \in \Omega = (\mathbf{X}_L, \mathbf{X}_R), t \in (T_0, T_f], \quad (4)$$

subject to the following initial and boundary conditions

$$\psi_j(\mathbf{X}, t = T_0) = \psi_j^{ic}, \quad \mathbf{X} \in \Omega, \quad (5)$$

$$\psi_j(\mathbf{X}, t) = \psi_j^{bc}, \quad (\mathbf{X}, t) \in \partial\Omega \times (T_0, T_f], \quad j = 1, 2. \quad (6)$$

In the problem setting above,  $\psi_j = \psi_j(\mathbf{X}, t)$  represents a complex-valued function of the spatial variables  $\mathbf{X} = (x, y)$  and the temporal variable  $t$ .  $\mathcal{N}$  is a nonlinear operator acting on the solutions  $\psi_j(\mathbf{X}, t)$  for  $j = 1, 2$ , their derivatives with respect to the spatial variables, and is parametrized by  $\lambda$ , which can be an unknown parameter (constant or variable). We also denote the domain of spatial variables by  $\Omega = [\mathbf{X}_L, \mathbf{X}_R]$  and the corresponding domain boundary by  $\partial\Omega$ , where  $\mathbf{X}_L = (x_L, y_L)$  and  $\mathbf{X}_R = (x_R, y_R)$  represent the left and right boundaries, respectively. The computational interval for the temporal variable  $t$  is also denoted by  $[T_0, T_f]$ . For  $j = 1, 2$ , physics models based on the left-hand side of Eq. (4) can be formulated as:

$$\begin{cases} \mathcal{F} := i\psi_{1,t} + \mathcal{N}[\psi_1, \psi_{1,\mathbf{X}}, \psi_{1,\mathbf{X}\mathbf{X}}, \dots; \lambda] = 0, \\ \mathcal{G} := i\psi_{2,t} + \mathcal{N}[\psi_2, \psi_{2,\mathbf{X}}, \psi_{2,\mathbf{X}\mathbf{X}}, \dots; \lambda] = 0. \end{cases} \quad (7)$$

Due to the complexity of the solutions  $\psi_j(\mathbf{X}, t)$ , we decompose them into the real and the imaginary parts as  $\psi_j(\mathbf{X}, t) = u_j(\mathbf{X}, t) + iv_j(\mathbf{X}, t)$ , where both  $u_j(\mathbf{X}, t)$  and  $v_j(\mathbf{X}, t)$  are real-valued functions. By considering the complex-valued physics models



as  $\mathcal{F} = \mathcal{F}_{u_1} + i\mathcal{F}_{v_1}$  and  $\mathcal{G} = \mathcal{G}_{u_2} + i\mathcal{G}_{v_2}$ , the system of equations (7) can be reformulated as follows:

$$\begin{cases} \mathcal{F}_{u_1} := u_{1,t} + \mathcal{N}_{u_1}[u_1, v_1, u_2, v_2, \dots; \lambda] = 0, \\ \mathcal{F}_{v_1} := v_{1,t} + \mathcal{N}_{v_1}[u_1, v_1, u_2, v_2, \dots; \lambda] = 0, \\ \mathcal{G}_{u_2} := u_{2,t} + \mathcal{N}_{u_2}[u_1, v_1, u_2, v_2, \dots; \lambda] = 0, \\ \mathcal{G}_{v_2} := v_{2,t} + \mathcal{N}_{v_2}[u_1, v_1, u_2, v_2, \dots; \lambda] = 0, \end{cases} \quad (8)$$

where  $\mathcal{N}_{u_1}$ ,  $\mathcal{N}_{v_1}$ ,  $\mathcal{N}_{u_2}$ , and  $\mathcal{N}_{v_2}$  are specified nonlinear operators of the real-valued functions  $u_1$ ,  $v_1$ ,  $u_2$ , and  $v_2$ , respectively. A PINN model aims to predict these real-valued functions by minimizing a multi-objective loss function which is designed to minimize the discrepancy between the model's predictions to the initial and boundary conditions (5) and (6), as well as the physical laws described by physics model in (8). The physics-informed part of the neural network model can be constructed using the provided physics models in (8), by differentiating the network's outputs with respect to the spatial and temporal variables using AD technique. Considering a three-dimensional input data  $\mathbf{z}^0 = (x, y, t)$  to the neural network model, a PINN model comprises a fully connected neural network with depth  $D$ ,  $D - 1$  hidden layers and an output layer. In each layer, we denote the number of neurons by  $N^\ell$  for  $\ell = 1, \dots, D$ . By feeding the input data into the network, an affine transformation will be applied as follows:

$$\mathcal{L}^\ell(\mathbf{z}^{\ell-1}) := \mathbf{w}^\ell \mathbf{z}^{\ell-1} + \mathbf{b}^\ell, \quad \ell = 1, \dots, D,$$

where  $\mathbf{z}^{\ell-1}$  is the input data from the previous layer to the next layer. Before sending the input data to the next layer, a nonlinear activation function  $\sigma^\ell(\cdot)$  should be applied component-wise to the transformed data of each layer. This activation function introduces nonlinearity into the model, allowing the neural network to capture complex patterns and relationships within the data. Common choices for the activation function include ReLU, sigmoid, or tanh, depending on the specific requirements of the problem being addressed [80]. In this paper, we use the tanh activation function for all our experiments.  $\mathbf{w}^\ell \in \mathbb{R}^{N^\ell \times N^{\ell-1}}$  and  $\mathbf{b}^\ell \in \mathbb{R}^{N^\ell}$  are the weight matrix and bias vector corresponding to the layer  $\ell$ , respectively. So, the final output of the neural network can be formed as

$$\hat{\psi}_{j,\boldsymbol{\theta}} := (\mathcal{L}^D \circ \sigma^{D-1} \circ \mathcal{L}^{D-1} \circ \dots \circ \sigma^1 \circ \mathcal{L}^1)_{(\mathbf{z}^0)},$$

where  $\boldsymbol{\theta} := \{\{\mathbf{w}^\ell, \mathbf{b}^\ell\}_{\ell=1}^D\}$  is the set of all trainable parameters, and the operator  $\circ$  is the composition operator. The PINNs model aims to predict the solutions to the system (4)-(6) by optimizing the network's trainable parameters. In doing so, we define the following mean square error (MSE) loss function, considering the residual forms of Eq. (5) and Eq. (6), along with the physics-informed component described by system (8)

$$Loss(\boldsymbol{\theta}) := Loss_{ic}(\boldsymbol{\theta}) + Loss_{bc}(\boldsymbol{\theta}) + Loss_r(\boldsymbol{\theta}), \quad (9)$$

where

$$Loss_{ic}(\boldsymbol{\theta}) := \frac{1}{N_{ic}} \sum_{k=1}^{N_{ic}} w_{ic}^{(k)} \left( \left| u_1^k - \hat{u}_{1,\boldsymbol{\theta}}(\mathbf{X}^k, t = T_0) \right|^2 + \left| v_1^k - \hat{v}_{1,\boldsymbol{\theta}}(\mathbf{X}^k, t = T_0) \right|^2 \right)$$



$$\begin{aligned}
& + \left| u_2^k - \hat{u}_{2,\boldsymbol{\theta}}(\mathbf{X}^k, t = T_0) \right|^2 + \left| v_2^k - \hat{v}_{2,\boldsymbol{\theta}}(\mathbf{X}^k, t = T_0) \right|^2, \\
Loss_{bc}(\boldsymbol{\theta}) := & \frac{1}{N_{bc}} \sum_{k=1}^{N_{bc}} w_{bc}^{(k)} \left( \left| u_1^k - \hat{u}_{1,\boldsymbol{\theta}}(\mathbf{X}^k, t^k) \right|^2 + \left| v_1^k - \hat{v}_{1,\boldsymbol{\theta}}(\mathbf{X}^k, t^k) \right|^2 \right. \\
& \left. + \left| u_2^k - \hat{u}_{2,\boldsymbol{\theta}}(\mathbf{X}^k, t^k) \right|^2 + \left| v_2^k - \hat{v}_{2,\boldsymbol{\theta}}(\mathbf{X}^k, t^k) \right|^2 \right),
\end{aligned}$$

and

$$\begin{aligned}
Loss_r(\boldsymbol{\theta}) := & \frac{1}{N_r} \sum_{j=1}^{N_r} w_r^{(j)} \left( \left| \mathcal{F}_{\hat{u}_{1,\boldsymbol{\theta}}}(\mathbf{X}^j, t^j) \right|^2 + \left| \mathcal{F}_{\hat{v}_{1,\boldsymbol{\theta}}}(\mathbf{X}^j, t^j) \right|^2 \right. \\
& \left. + \left| \mathcal{G}_{\hat{u}_{2,\boldsymbol{\theta}}}(\mathbf{X}^j, t^j) \right|^2 + \left| \mathcal{G}_{\hat{v}_{2,\boldsymbol{\theta}}}(\mathbf{X}^j, t^j) \right|^2 \right),
\end{aligned}$$

where  $\left\{ (\mathbf{X}^k, t = T_0), u_1^k, v_1^k, u_2^k, v_2^k \right\}_{k=1}^{N_{ic}}$  and  $\left\{ (\mathbf{X}^k, t^k), u_1^k, v_1^k, u_2^k, v_2^k \right\}_{k=1}^{N_{bc}}$  are the sets of training data corresponding to the initial and boundary conditions, respectively. We also denote the set of residual points by  $\left\{ (\mathbf{X}^k, t^k) \right\}_{k=1}^{N_r}$  for the residual networks  $\mathcal{F}_{\hat{u}_{1,\boldsymbol{\theta}}}$ ,  $\mathcal{F}_{\hat{v}_{1,\boldsymbol{\theta}}}$ ,  $\mathcal{G}_{\hat{u}_{2,\boldsymbol{\theta}}}$ , and  $\mathcal{G}_{\hat{v}_{2,\boldsymbol{\theta}}}$ . These points can be sampled either uniformly or randomly.  $w_{ic}$ ,  $w_{bc}$ , and  $w_r$  are point-specific weights that specify different weights assigned to the initial condition, boundary condition, and residual loss terms in the overall loss function. These weights allow for fine-tuning the relative importance of each component, enabling the model to balance the accuracy of the predictions across the different aspects of the problem. Then, the optimal values of the network's parameters can be obtained by minimizing the MSE loss function (9) using variants of gradient descent algorithm (e.g., SGD and Adam) [81, 82], or other classes of optimization algorithms. The corresponding complex-valued physics-informed part of the PINN model for the  $(2+1)$ -dimensional VC-CNLSE (3) can be formulated as follows:

$$\begin{cases} \mathcal{F}_{u_1} := -v_{1,t} + \alpha(t)(u_{1,xx} + u_{1,yy}) + \beta(t)(u_1^2 + v_1^2 + u_2^2 + v_2^2)u_1 = 0, \\ \mathcal{F}_{v_1} := u_{1,t} + \alpha(t)(v_{1,xx} + v_{1,yy}) + \beta(t)(u_1^2 + v_1^2 + u_2^2 + v_2^2)v_1 = 0, \\ \mathcal{G}_{u_2} := -v_{2,t} + \alpha(t)(u_{2,xx} + u_{2,yy}) + \beta(t)(u_1^2 + v_1^2 + u_2^2 + v_2^2)u_2 = 0, \\ \mathcal{G}_{v_2} := u_{2,t} + \alpha(t)(v_{2,xx} + v_{2,yy}) + \beta(t)(u_1^2 + v_1^2 + u_2^2 + v_2^2)v_2 = 0. \end{cases} \quad (10)$$

A major drawback of neural network-based approaches is their slow training, which can affect the convergence speed and performance of the underlying model. To address this issue, a locally adaptive activation function is introduced [78], in which scalable parameters are defined to increase the slope of the activation functions. This further reduces the risk of vanishing gradients and improves the convergence speed, resulting in lower training costs. For a neural network model parametrized by  $\boldsymbol{\theta}$ , the neuron-wise scalable parameters  $na$  can act as

$$\sigma^\ell(na_k^\ell(\mathcal{L}^\ell(z^{\ell-1})))_k, \quad \ell = 1, \dots, D-1, \quad k = 1, \dots, N^\ell,$$

where  $n \geq 1$  is a pred-defined scalable factor. This configuration will introduce additional  $\sum_{\ell=1}^{D-1} N^\ell$  trainable parameters to be optimized, where each neuron in each hidden layer has its own slope for the activation function. Then, the set of trainable parameters  $\boldsymbol{\theta}$  consists of the set of weights and biases  $\{(\mathbf{w}^\ell, \mathbf{b}^\ell)\}_{\ell=1}^D$  and the set of scalable parameters  $\{a_k^\ell\}_{\ell=1}^{D-1}, \forall k = 1, \dots, N^\ell$ . We initialize these scalable parameters such that  $na_k^\ell = 1, \forall n \geq 1$ . In order to force the network to quickly increase the slope of the activation function, we define a slope recovery loss term to be added into the overall loss function as:

$$Loss_a := \frac{1}{\frac{1}{D-1} \sum_{\ell=1}^{D-1} \exp(\frac{\sum_{k=1}^{N^\ell} a_k^\ell}{N^\ell})}.$$

Hence, the loss function (9) can be reformulated as follows:

$$Loss(\boldsymbol{\theta}) := Loss_{ic}(\boldsymbol{\theta}) + Loss_{bc}(\boldsymbol{\theta}) + Loss_r(\boldsymbol{\theta}) + w_a \cdot Loss_a(\boldsymbol{\theta}). \quad (11)$$

where  $w_a$  is a user-defined hyper-parameter weight for the individual loss function corresponding to the slope recovery term.

In applying the proposed PINN framework for data-driven solution and parameter discovery to the model equation (3), the loss function (11) ensures that the model predictions satisfy the observed data corresponding to the initial and boundary conditions, as well as the physics-informed parts provided by the system of equations (10). In general, for a PINN model, the behavior of the equation residuals often exhibits many oscillations around zero. Indeed, the underlying PINN model aims to force the equation residuals to zero by penalizing these residuals at so-called collocation points, which are sampled uniformly or randomly within the computational domain. The residual-based adaptive refinement (RAR) strategy is proposed to address this issue. The RAR strategy focuses on regions of the computational domain where the residuals are largest. This approach improves the distribution of residual points by adaptively sampling more points in these regions during the training phase. In all our experiments, we randomly sample  $m$  new residual points after specific training iterations until either the maximum number of iterations is reached or the value of the residuals falls below a predefined threshold. This motivates us to define region-specific weight  $w_r^{reg}$  instead of point-specific one for individual residual loss term in Eq. (11), corresponding to the physics-informed parts described by the governing equations.

For the system (3), we combine the proposed PINN framework with the RAR technique to demonstrate that each residual, as described in the system of equations (10), requires a different distribution of residual points. To evaluate the performance and accuracy of our method, we consider two metrics, the  $\mathbb{L}^2$  error and the point-wise error, defined as follows:

$$Error_{\mathbb{L}^2} := \frac{\left( \sum_{k=1}^N \left| \psi_j(\mathbf{X}^k, t^k) - \hat{\psi}_{j,\boldsymbol{\theta}}(\mathbf{X}^k, t^k) \right|^2 \right)^{1/2}}{\left( \sum_{k=1}^N \left| \psi_j(\mathbf{X}^k, t^k) \right|^2 \right)^{1/2}},$$

$$Error_{pw} := \frac{|\psi_j(\mathbf{X}^k, t^k) - \hat{\psi}_{j,\theta}(\mathbf{X}^k, t^k)|}{|\psi_j(\mathbf{X}^k, t^k)|}, \quad j = 1, 2,$$

where  $\psi_j(\cdot, \cdot)$  and  $\hat{\psi}_{j,\theta}(\cdot, \cdot)$  are the exact and predicted solutions, respectively, evaluated at sampled test points. The  $\mathbb{L}^2$  error measures the overall deviation between the exact and predicted solutions across the entire domain, while the point-wise error assesses the deviation at specific points of interest. The architecture of the proposed PINN framework is depicted in Fig 1. Since we are working in a two-dimensional space, the input layer should be adjusted to include both spatial and temporal coordinates, which induces a three-dimensional problem solving. The input data is transformed by applying the weights and biases to each neuron in each hidden layer. An adaptive nonlinear activation function is then applied component-wise to the transformed data, activating each neuron. Each neuron in the previous layer is fully connected to the neurons in the next layer. In the output layer, there are four neurons, corresponding to the predictions for the system (3), which include the real and imaginary parts of the decomposed solutions. After the network's outputs are obtained, the network is able to construct the physics-informed parts through the application of the AD technique. For this, the values of the variable coefficients must be computed first. Then, the physics-informed neural network can be constructed using the residuals provided by the physics models in (10). Both networks share their parameters during training. By constructing the loss functions corresponding to the governing equations, initial and boundary conditions, and the slope recovery loss, one can repeatedly obtain the optimal values of the network's parameters by minimizing the overall loss function using appropriate optimization algorithms. In this paper, the loss functions are optimized using both the Adaptive Moment Estimation (Adam) and Limited-Memory Broyden-Fletcher-Goldfarb-Shanno (L-BFGS) algorithms. Adam is a gradient-based optimization algorithm that combines the advantages of two other extensions of stochastic gradient descent algorithm. It maintains adaptive learning rates for each parameter by computing first and second moments of the gradients. On the other hand, L-BFGS is a full-batch quasi-Newton method known for its effectiveness in optimizing functions by approximating the inverse Hessian matrix [83]. Combining these two methods leverages Adam's robustness and adaptability in the initial stages of training with L-BFGS's precision in fine-tuning the final solution. This minimization process will continue until the network's error falls below a pre-defined threshold  $\delta$  or the maximum number of iterations is reached. We initialize the network's parameters using Xavier initialization technique. We sketch the proposed PINN algorithm for solving the  $(2+1)$ -dimensional VC-CNLSE in Algorithm 1. In all our experiments, we initialize the scalable parameters such that  $n = 5$  and  $a_k^\ell = 0.2$  for  $\ell = 1, \dots, D-1$  and  $k = 1, \dots, N^\ell$ . We set the initial condition loss, boundary condition loss, and slope recovery loss weights as:  $w_{ic} = 1$ ,  $w_{bc} = 1$ , and  $w_a = \frac{1}{100}$ . Setting  $w_a = \frac{1}{100}$  ensures that the value of the loss is not too large. We generate the residual points randomly using Latin Hypercube Sampling (LHS) strategy [84] within the computational domain. We start training the constructed PINN model with an initial number of residual points, setting  $m = 25$ . After 5000 iterations, we add  $2^k \times m$  ( $k = 1, 2, 3, \dots$ )

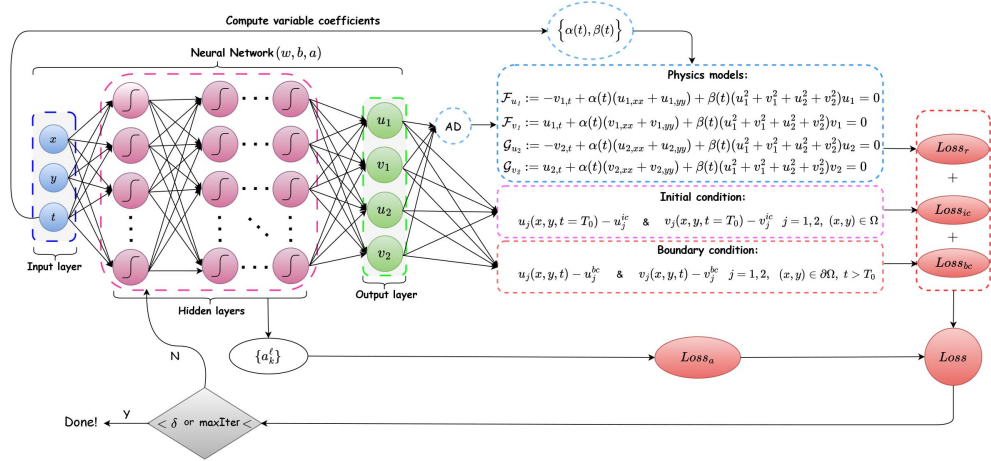


**Fig. 1** The architecture of the proposed PINN for the  $(2+ 1)$ -dimensional VC-CNLSE.

new residual points for each residual equations based on the RAR algorithm during the training phase. This approach helps to reduce the oscillations in the residual equations while using fewer residual points. The accompanying code for this paper is written in Python, and the numerical results are reported using the JAX library. The JAX library is used for its efficient automatic differentiation and high-performance numerical computing capabilities. The library's Just-In-Time (JIT) compilation and automatic differentiation features significantly enhance the performance and accuracy of the computations involved in solving complex differential equations. The computations were performed on a Lenovo Legion laptop equipped with a 2.30 GHz Intel Core i7-11800H processor and a single NVIDIA GeForce RTX 3060 GPU card.

### 3 Results and discussions

In this section, we apply the proposed PINN framework to the  $(2+ 1)$ -dimensional VC-CNLSE and assess its accuracy and performance in predicting various soliton dynamics. First, we address the problem of data-driven soliton solutions to the model equation, predicting phenomena such as vector parabolic dark one-soliton, vector m-shaped anti-dark one-soliton, and dark two-solitons. By considering different formations of dispersion and nonlinearity coefficients, we demonstrate that our method is capable of predicting the corresponding soliton dynamics with high accuracy. Second, we explore the parameter discovery within the model equation, focusing on accurately identifying both constant and variable coefficients.

#### 3.1 Data-driven solution to $(2+ 1)$ -dimensional VC-CNLSE

Choosing different and appropriate formations of dispersion and nonlinearity coefficients leads us to explore a wide range of soliton dynamics and behaviors. By adjusting

---

**Algorithm 1** Enhanced PINN algorithm to  $(2+1)$ -dimensional VC-CNLSE

---

**Require:**

- Training data sets  $\left\{(\mathbf{X}^k, T_0), u_1^k, v_1^k, u_2^k, v_2^k\right\}_{k=1}^{N_{ic}}$  and  $\left\{(\mathbf{X}^k, t^k), u_1^k, v_1^k, u_2^k, v_2^k\right\}_{k=1}^{N_{bc}}$
- Residual points  $\left\{(\mathbf{X}^k, t^k)\right\}_{k=1}^{N_r}$
- The value of the hyper-parameters  $\delta, m, n, w_a$
- Construct a neural network model with Xiavier initialization technique

**while** (error  $< \delta$  or nIter  $< \maxIter$ ) **do**

(a) Construct the physics-informed neural network by computing the variable coefficients and incorporating the network's predictions into the physics models using the AD technique.

(b) Specification of the overall loss function  $Loss(\boldsymbol{\theta})$  using the losses corresponding to the governing equations, initial and boundary conditions, and the slope recovery loss function.

(c) Add  $m$  new residual points for each residual equation based on the RAR technique, where

$$\arg \max_{(\mathbf{X}, t)} \left\{ |\mathcal{F}_{u_1}|, |\mathcal{F}_{v_1}|, |\mathcal{G}_{u_2}|, |\mathcal{G}_{v_2}| \right\}$$

(d) Find the optimal values of the network's parameters by minimizing the overall loss function using an appropriate optimization algorithm.

**end while**

---

these coefficients, we can model various physical scenarios and validate the robustness and versatility of our proposed PINN framework. This capability highlights the framework's potential to be applied to complex, real-world problems where the underlying physics is governed by variable coefficients. In doing so, we consider the equation system (3) equipped with the initial condition (5) and the boundary condition (6).

### 3.1.1 Discovery of one-soliton solutions

By applying the Hirota method, one can obtain the following one-soliton solutions [25]:

$$\psi_1(x, y, t) = \mu \frac{e^{ib(t)(1+e^{\xi(x,y,t)+2i\theta})}}{1 + e^{\xi(x,y,t)}}, \quad \psi_2(x, y, t) = \lambda \frac{e^{ib(t)(1+e^{\xi(x,y,t)+2i\theta})}}{1 + e^{\xi(x,y,t)}}, \quad (12)$$

where

$$b(t) := (|\lambda|^2 + |\mu|^2) \int \beta(t) dt, \quad (13)$$

$$\beta(t) := -\frac{\csc^2(\theta)(k^2 + m^2)\alpha(t)}{2(|\lambda|^2 + |\mu|^2)}, \quad (14)$$

$$w(t) := \cot(\theta)(k^2 + m^2) \int \alpha(t) dt, \quad (15)$$

$$\xi(x, y, t) := kx + my + w(t) + \delta. \quad (16)$$

Here,  $k$ ,  $m$ , and  $\delta$  are real constants.  $\lambda$  and  $\mu$  are complex constants, while  $\theta$  is a real phase shift. One can see that the one-soliton solutions (12) are proportional to each other. This leads us to dealing with a Manakov system when we set  $\tau = 1$  in the system of equations (3).

- Parabolic vector dark one-soliton

Based on the solutions (12), the parabolic vector dark one-soliton for the  $(2+1)$ -dimensional VC-CNLSE (3) can be obtained by taking  $k = -1.4, m = 1.1, \delta = 1, \mu = -2, \theta = 3.8, \lambda = -2$ , and  $\alpha(t) = t$ . With this configuration, one can see that the amplitudes for both  $\psi_1$  and  $\psi_2$  are the same. We set the spatial domain  $\Omega = [-10, 10] \times [-10, 10]$  and the temporal domain  $[-1, 1]$ . Then, the initial and boundary conditions on these regions can be obtained as:

$$\begin{cases} \psi_j(x, y, t = -1) = -2 \frac{e^{ib(-1)}(1+e^{\xi(x, y, -1)+i7.6})}{1+e^{\xi(x, y, -1)}}, & (x, y) \in \Omega, \\ \psi_j(x = -10, y, t) = -2 \frac{e^{ib(t)}(1+e^{\xi(-10, y, t)+i7.6})}{1+e^{\xi(-10, y, t)}}, & (y, t) \in [-10, 10] \times (-1, 1], \\ \psi_j(x, y = -10, t) = -2 \frac{e^{ib(t)}(1+e^{\xi(x, -10, t)+i7.6})}{1+e^{\xi(x, -10, t)}}, & (x, t) \in [-10, 10] \times (-1, 1], \\ \psi_j(x = 10, y, t) = -2 \frac{e^{ib(t)}(1+e^{\xi(10, y, t)+i7.6})}{1+e^{\xi(10, y, t)}}, & (y, t) \in [-10, 10] \times (-1, 1], \\ \psi_j(x, y = 10, t) = -2 \frac{e^{ib(t)}(1+e^{\xi(x, 10, t)+i7.6})}{1+e^{\xi(x, 10, t)}}, & (x, t) \in [-10, 10] \times (-1, 1], \quad j = 1, 2. \end{cases}$$

Based on the information above, we first generate the training dataset corresponding to the initial and boundary conditions. We randomly generate  $N_{ic} = 100$  initial points and  $N_{bc} = 100$  boundary points. Beyond that, we divide the computational domain  $\Omega \times [-1, 1]$  into  $256 \times 256 \times 201$  discrete equidistant points to test the accuracy of the underlying PINN model. In order to inform the physics models (10) into the neural network's knowledge, we use the LHS technique to generate  $N_r = 10,000$  residual points. These points are used to penalize the physics models at the so-called collocation points. Then, the overall loss function can be constructed by considering the MSE losses corresponding to the initial and boundary conditions, the physics models, and the loss associated with the slope recovery. For this problem, we consider a neural network model with 5 hidden layers and 40 neurons in each layer. We start by training our model with 30,000 iterations of the Adam optimizer with the default learning rate to minimize the corresponding loss function. Then, we continue to obtain the optimal values of the network's parameters by performing 5,144 iterations of the L-BFGS optimizer. The training time was recorded as 1729.6354 s and 780.5243 s for the Adam optimizer and the L-BFGS optimizer, respectively. After 30,000 iterations of the Adam optimizer, the  $\mathbb{L}^2$  relative errors for the solutions  $\psi_1$  and  $\psi_2$  are measured as 0.18% and 0.19%. By continuing the optimization using the L-BFGS optimizer, the  $\mathbb{L}^2$  relative errors decrease to 0.073% and 0.064%, respectively. After all, we are able to plot the obtained results from the trained PINN model.

Using the RAR strategy, we first train the underlying model with  $N_f = 10,000$  residual points and then gradually add 6,200 new points during the training. As depicted in the first column of Fig. 2, the added residual points corresponding to the residual equations have different distributions. It means that each residual equation

in (10) has its own characteristics, and this importance should be considered when applying PINN methods to such model equations. The three-dimensional plots of point-wise errors for the solution  $\psi_1$  along the  $x - y$  axis at two temporal levels,  $t = -1$  and  $t = 1$ , are depicted in the second and third columns of Fig. 2, respectively. One can see that using RAR drastically decreases the prediction errors and leads residual equations to have uniform distributions of residual points. This phenomenon can be addressed by forcing the residuals to zero during training. In Fig. 3, the density plots of the exact and predicted dynamics, as well as the comparison between the exact and predicted solutions for  $\psi_1$  at different temporal levels, are depicted. In the top row, the density plots along the  $x - t$  plane at  $y = 0$  and  $y - t$  plane at  $x = 0$  are shown, where the pulse propagates parabolically with opposite directions in  $x - t$  and  $y - t$  planes. In the middle row, the density plots of the exact and predicted dynamics at two temporal levels,  $t = -1$  and  $t = 1$ , along the  $x - y$  plane are depicted. One can observe that the pulse propagates along a straight line. A comparison between the exact and predicted solutions at four temporal levels for  $x = 10$  and  $y = 10$  is presented in the bottom row. These results show that the trained PINN model can accurately capture the exact dynamics in the  $x - t$ ,  $y - t$ , and  $x - y$  planes, demonstrating the robustness of our method. The evolution of the parabolic dark one-soliton in the  $x - t$  plane (first row) at  $y = -8$ ,  $y = 0$ , and  $y = 8$  (from left to right) and in the  $y - t$  plane (bottom row) at  $x = -8$ ,  $x = 0$ , and  $x = 8$  (from left to right) is illustrated in Fig. 4. The behavior of the loss functions during training with 30,000 iterations of the Adam optimizer and 5,144 iterations of the L-BFGS optimizer is depicted in Fig. 5. From the left panel one can see that the Adam optimizer exhibits a slowly decreasing loss with several oscillations during training. The loss values after training with the Adam optimizer are recorded as follows:  $1.337e - 2$  for the overall loss function,  $1.732e - 4$  for the initial condition loss function,  $3.283e - 4$  for the boundary condition loss function, and  $6.014e - 3$  for the residual loss function. From the middle panel of Fig. 5 one can see that the oscillatory behavior of the MSE loss for each individual residual equation is relatively close to others. In contrast, the L-BFGS optimizer exhibits smoother behavior of the loss curves without any oscillations as depicted in the right panel of Fig. 5. The loss values after training with the L-BFGS optimizer are recorded as follows:  $8.483e - 03$  for the overall loss function,  $4.587e - 6$  for the initial condition loss function,  $6.705e - 6$  for the boundary condition loss function, and  $9.559e - 5$  for the residual loss function. It should be noted that, in comparison with the results obtained from the Adam optimizer, the L-BFGS optimizer demonstrates a faster convergence framework.

- Vector m-shaped anti-dark one-soliton

Taking  $k = -0.19$ ,  $m = -1.5$ ,  $\delta = 1$ ,  $\mu = -1.1 + i$ ,  $\theta = -4.1$ ,  $\lambda = -1.1 + i$ , and  $\alpha(t) = t \ln t^2$  in (12)-(16), one can obtain the vector m-shaped anti-dark one-soliton solution to the  $(2 + 1)$ -dimensional VC-CNLSE [25]. Based on these configurations, one can see that the amplitudes for both  $\psi_1$  and  $\psi_2$  are the same. We set the spatial domain as  $\Omega = [-25, 25] \times [-4, 4]$  and the temporal domain as  $[-2, 2]$ . In order to generate the training data corresponding to the initial and boundary conditions, for



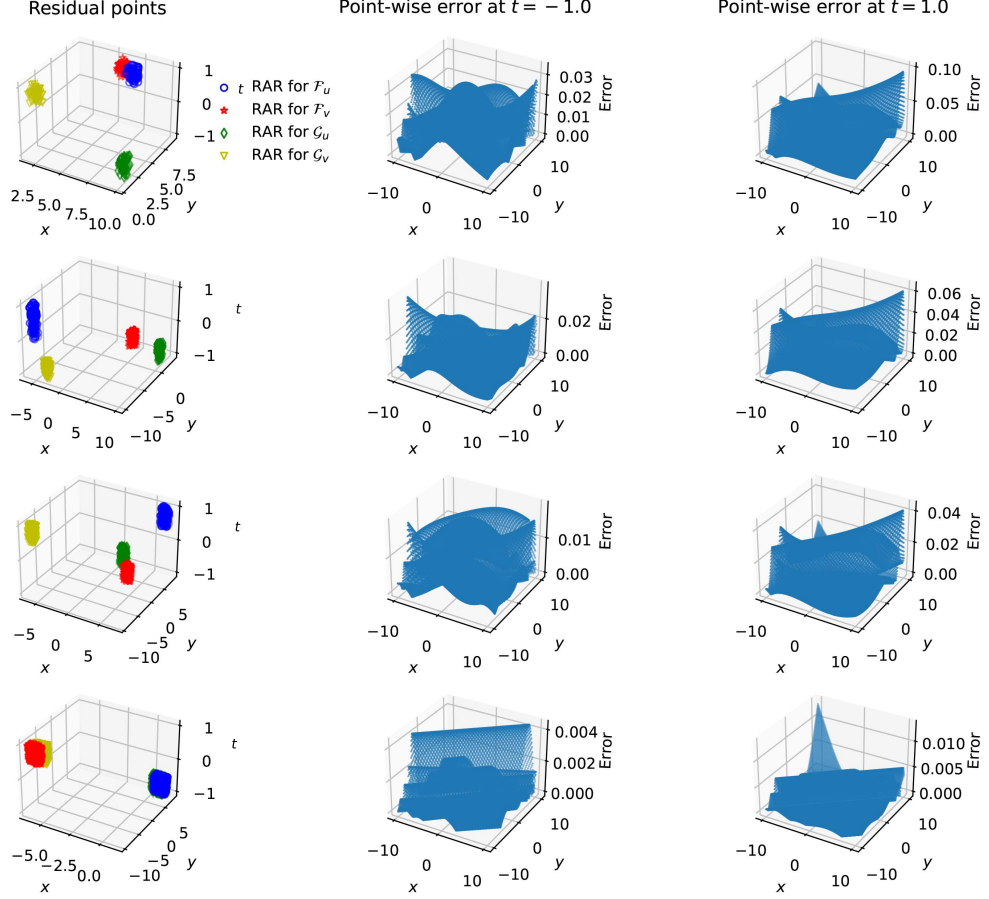


**Fig. 2** The distribution of added new residual points (first column) and the point-wise errors of  $\psi_1$  (second and third columns).

$j = 1, 2$  we consider the following equations:

$$\begin{cases} \psi_j(x, y, t = -2) = (-1.1 + i) \frac{e^{ib(-2)}(1 + e^{\xi(x, y, -2) - i8.2})}{1 + e^{\xi(x, y, -2)}}, & (x, y) \in \Omega, \\ \psi_j(x = -25, y, t) = (-1.1 + i) \frac{e^{ib(t)}(1 + e^{\xi(-25, y, t) - i8.2})}{1 + e^{\xi(-25, y, t)}}, & (y, t) \in [-4, 4] \times (-2, 2], \\ \psi_j(x, y = -4, t) = (-1.1 + i) \frac{e^{ib(t)}(1 + e^{\xi(x, -4, t) - i8.2})}{1 + e^{\xi(x, -4, t)}}, & (x, t) \in [-25, 25] \times (-2, 2], \\ \psi_j(x = 25, y, t) = (-1.1 + i) \frac{e^{ib(t)}(1 + e^{\xi(25, y, t) - i8.2})}{1 + e^{\xi(25, y, t)}}, & (y, t) \in [-4, 4] \times (-2, 2], \\ \psi_j(x, y = 4, t) = (-1.1 + i) \frac{e^{ib(t)}(1 + e^{\xi(x, 4, t) - i8.2})}{1 + e^{\xi(x, 4, t)}}, & (x, t) \in [-25, 25] \times (-2, 2]. \end{cases}$$

We divide the computational domain  $\Omega \times [-2, 2]$  into  $256 \times 256 \times 200$  discrete equidistant points to create a dataset for testing the performance of the underlying PINN model. We randomly generate  $N_{ic} = 100$  and  $N_{bc} = 100$  training points corresponding to the initial and boundary conditions, respectively. We also use the

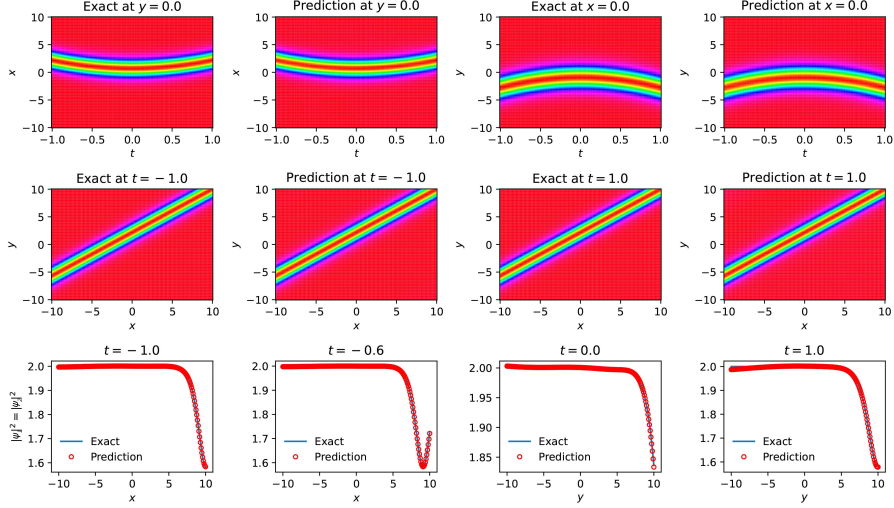


**Fig. 3** The density plots of the exact and predicted dynamics (top and middle rows) and the comparison between the exact and predicted solutions at different temporal levels (bottom row).

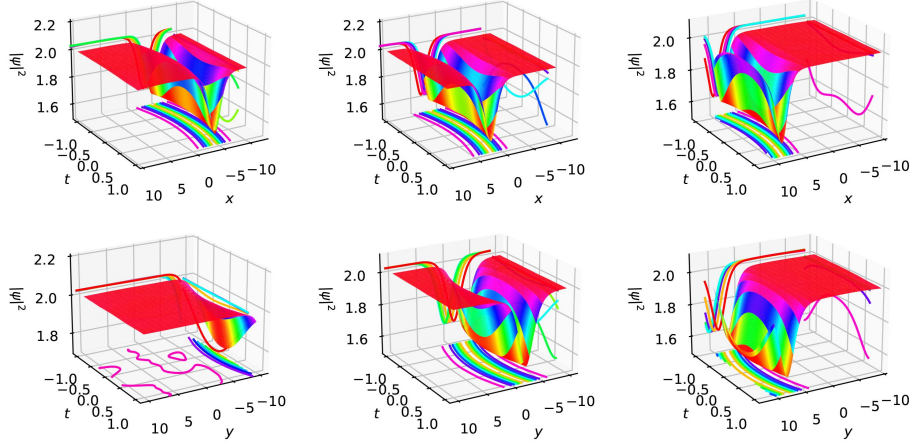


**Fig. 4** Three-dimensional plots with contour map of the predicted dynamics for  $\psi_j$  in the  $x-t$  (top row) and  $y-t$  (bottom row) planes.

LHS technique to generate  $N_r = 10,000$  residual points within the computational domain. Then, a PINN model based on the enhanced framework, equipped with a neural network consisting of 5 hidden layers and 40 neurons per layer, is going to be trained with  $N_r = 10,000$  residual points. Using the RAR strategy, we gradually add 6,200 residual points during training. After 30,000 iterations with the Adam optimizer and 5,170 iterations with the L-BFGS optimizer, we are ready to recover the m-shaped anti-dark one-soliton solutions using the trained model. The  $\mathbb{L}^2$  relative errors for the solutions  $\psi_1$  and  $\psi_2$  are reduced from 6.4% and 6.4% to 0.29%

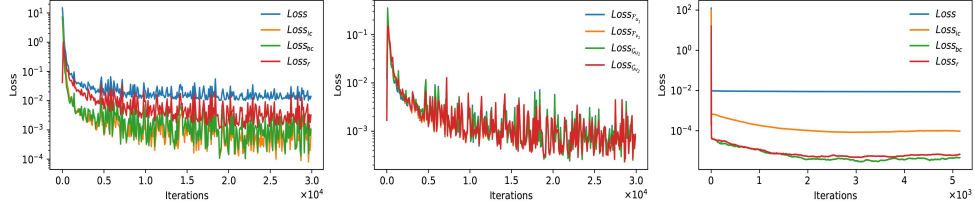


**Fig. 5** The loss curves during the training with 30,000 iterations of the Adam optimizer (left and middle panels) and the loss curves with 5,144 iterations of the L-BFGS optimizer (right panel).

and 0.28%, respectively, by using the Adam optimizer and then continuing the optimization process with the L-BFGS optimizer. The training times are recorded as 1412.4702 s and 740.1036 s for the Adam and L-BFGS optimizers, respectively. In Fig. 6, the density plots of the exact and predicted soliton dynamics are shown in the top and middle rows. It can be seen from the top row that our model is able to successfully capture the m-shaped dynamics of the anti-dark one-soliton solution. These dynamics exhibit an m-shaped pulse propagation with two smooth crests in the  $x - t$  and  $y - t$  planes. One can observe that the two crests in the  $x - t$  plane are wider than those in the  $y - t$  plane. On the other hand, the pulse propagates in the  $x - y$  plane along a straight line, as depicted in the middle row. A comparison between the exact and predicted dynamics is presented at different temporal levels for  $y = 4$  and  $x = 25$  in the bottom row to show the accuracy of the trained model. The evolution of the m-shaped anti-dark one-soliton solution and the corresponding point-wise errors in the  $x - t$  and  $y - t$  planes are depicted in Fig. 7 for  $x = 0$  and  $y = 0$  through three-dimensional plots. In Fig. 8, the loss curves during training with 30,000 iterations of the Adam optimizer and 5,170 iterations of the L-BFGS optimizer are illustrated. As expected, the Adam optimizer exhibits a slow decrease in loss values with many oscillations during training. From the middle panel of Fig. 8, the MSE loss for each individual residual equation oscillates relatively close to one another. On the other hand, the loss values exhibit smooth behavior without any oscillations when using the L-BFGS optimizer, as shown in the right panel of Fig. 8. The loss values after training with the Adam optimizer are recorded as follows:  $1.521e - 02$  for the overall loss function,  $1.118e - 03$  for the initial condition loss function,  $3.675e - 04$  for the boundary condition loss function, and  $5.034e - 03$  for the residual loss function. The loss values after training with the L-BFGS optimizer are recorded as follows:  $8.881e - 03$  for the overall loss function,  $2.622e - 06$  for the initial condition loss function,  $1.184e - 05$  for the boundary condition loss function, and  $2.571e - 04$  for the residual loss function. These results show that the L-BFGS optimizer achieves lower loss values across all categories compared to the Adam optimizer. Specifically, the L-BFGS optimizer demonstrates superior performance in minimizing the residual loss function and initial condition loss function, reflecting its efficiency in converging to a more accurate solution with fewer oscillations. This indicates that the L-BFGS optimizer provides a more stable and effective framework for training the PINN model in this context.

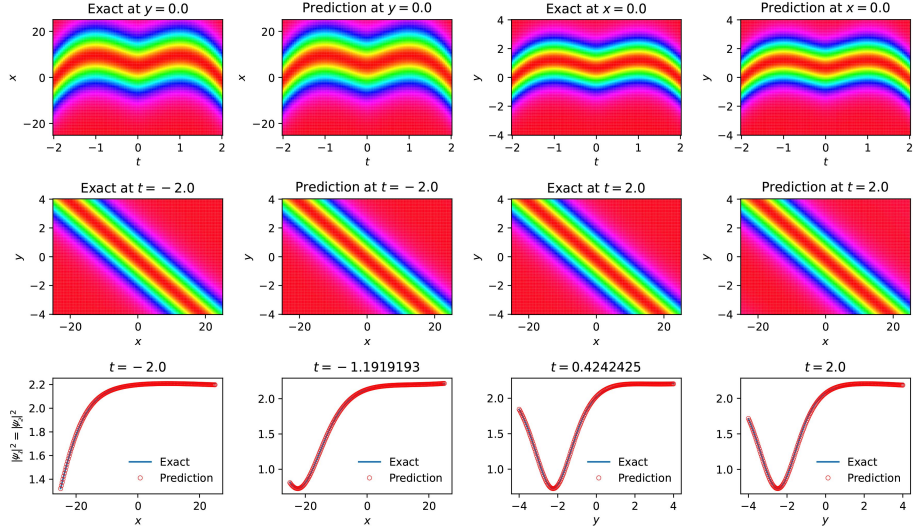


**Fig. 6** The density plots of the exact and predicted dynamics (top and middle rows) and the comparison between the exact and predicted solutions at different temporal levels (bottom row).

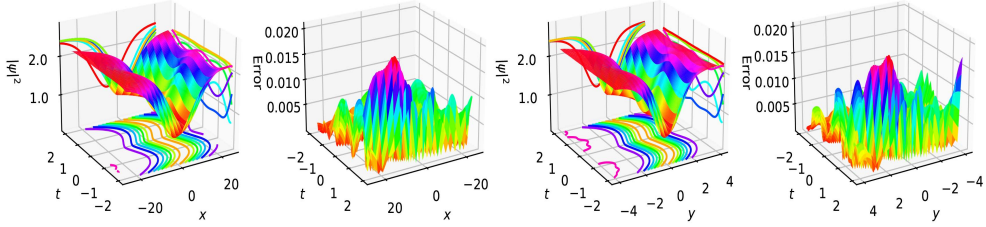


**Fig. 7** Three-dimensional plots with contour maps and the corresponding point-wise errors for  $\psi_j$  in the  $x-t$  plane (first and second panels) and  $y-t$  plane (third and fourth panels), from left to right.

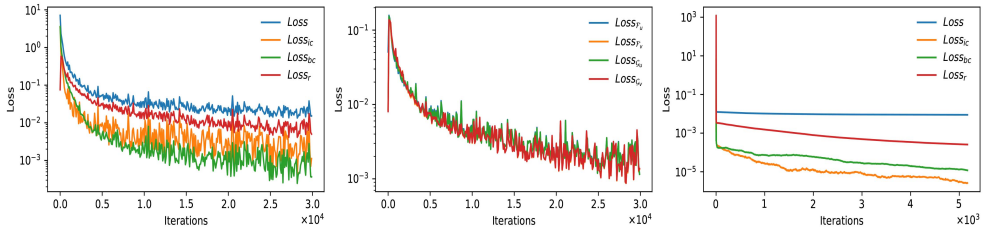


**Fig. 8** The loss curves during the training with 30,000 iterations of the Adam optimizer (left and middle panels) and the loss curves with 5,170 iterations of the L-BFGS optimizer (right panel).

### 3.1.2 Discovery of two-soliton solutions

The general form of the dark two-soliton solutions for the system of equations (3) can be obtained by applying the Hirota method as follows [57]:

$$\psi_1 = \mu e^{ib(t)} \frac{1 + e^{\xi_1(x,y,t)+i2\theta_1} + e^{\xi_2(x,y,t)+i2\theta_2} + \hat{B}e^{\xi_1(x,y,t)+\xi_2(x,y,t)+i2\theta_1+i2\theta_2}}{1 + e^{\xi_1(x,y,t)} + e^{\xi_2(x,y,t)} + \hat{A}e^{\xi_1(x,y,t)+\xi_2(x,y,t)}}, \quad (17)$$

$$\psi_2 = \lambda e^{ib(t)} \frac{1 + e^{\xi_1(x,y,t)+i2\theta_1} + e^{\xi_2(x,y,t)+i2\theta_2} + \hat{C}e^{\xi_1(x,y,t)+\xi_2(x,y,t)+i2\theta_1+i2\theta_2}}{1 + e^{\xi_1(x,y,t)} + e^{\xi_2(x,y,t)} + \hat{A}e^{\xi_1(x,y,t)+\xi_2(x,y,t)}}, \quad (18)$$

where

$$k := \eta(|\mu|^2 + |\lambda|^2), \quad \sigma_2 := \frac{|\sin(\theta_2)|}{|\sin(\theta_1)|}\sigma_1, \quad b(t) := -k \int \alpha(t)dt, \quad (19)$$

$$\rho_1 := \sqrt{2k \sin^2(\theta_1) - \sigma_1^2}, \quad \rho_2 := \sqrt{2k \sin^2(\theta_2) - \sigma_2^2}, \quad (20)$$

$$w_1(t) := k \sin(2\theta_1) \int \alpha(t)dt, \quad w_2(t) := k \sin(2\theta_2) \int \alpha(t)dt, \quad (21)$$

$$\hat{A} = \hat{B} = \hat{C} := \frac{\sigma_1\sigma_2 + \rho_1\rho_2 - 2k \sin(\theta_1) \sin(\theta_2) \cos(\theta_1 - \theta_2)}{\sigma_1\sigma_2 + \rho_1\rho_2 - 2k \sin(\theta_1) \sin(\theta_2) \cos(\theta_1 + \theta_2)}, \quad (22)$$

$$\xi_1(x, y, t) := \sigma_1 x + \rho_1 y + w_1(t), \quad \xi_2(x, y, t) := \sigma_2 x + \rho_2 y + w_2(t). \quad (23)$$

Here,  $\eta$ ,  $\sigma_1$ ,  $\sigma_2$ ,  $\rho_1$ ,  $\rho_2$ ,  $\hat{A}$ ,  $\hat{B}$ , and  $\hat{C}$  are all real constants,  $\mu$  and  $\lambda$  are complex constants, and  $\theta_1$  and  $\theta_2$  are the real ones and can be varied within the range  $[0, 2\pi]$ .  $w_1(t)$  and  $w_2(t)$  are real functions of the temporal variable  $t$ . It has been investigated that the amplitudes of the two circularly polarized waves are affected by  $\mu$  and  $\lambda$ .

- Parallel dark two-solitons

By setting the perturbation coefficient  $\alpha(t) = \frac{1}{2}t$ , and choosing the other constants as  $\eta = 1$ ,  $\sigma_1 = 1$ ,  $k = 4$ ,  $\mu = \lambda = 1 + i$ ,  $\theta_1 = \frac{\pi}{4}$ , and  $\theta_2 = \frac{\pi}{3}$  in (17)-(23), one can obtain the parallel dark two-soliton solutions to the (2+1)-dimensional VC-CNLSE (3). The nonlinearity coefficient can be considered proportional to the dispersion coefficient, expressed as  $\beta(t) = -\eta\alpha(t)$ . For data-driven dark two-soliton solutions to the model equation (3), we consider the spatial and temporal domains as  $\Omega = [-8, 8] \times [-6, 6]$  and  $[-0.1, 0.1]$ , respectively. In order to generate the initial and boundary training dataset, we consider the following equations

$$\begin{cases} \psi_j(x, y, t = -0.1) = \psi_j^{ic}(x, y, t = -0.1), & (x, y) \in \Omega, \\ \psi_j(x = -8, y, t) = \psi_j^{bc}(x = -8, y, t), & (y, t) \in [-6, 6] \times (-0.1, 0.1], \\ \psi_j(x, y = -6, t) = \psi_j^{bc}(x, y = -6, t), & (x, t) \in [-8, 8] \times (-0.1, 0.1], \\ \psi_j(x = 8, y, t) = \psi_j^{bc}(x = 8, y, t), & (y, t) \in [-6, 6] \times (-0.1, 0.1], \\ \psi_j(x, y = 6, t) = \psi_j^{bc}(x, y = 6, t), & (x, t) \in [-8, 8] \times (-0.1, 0.1], \quad j = 1, 2, \end{cases}$$

where  $\psi_j^{ic}$  and  $\psi_j^{bc}$  can be constructed using the solutions provided in (17) and (18) for  $j = 1, 2$ . First of all, we divide the computational domain  $\Omega \times [-0.1, 0.1]$

into  $256 \times 256 \times 201$  discrete equidistant points. We randomly generate  $N_{ic} = 200$  initial points and  $N_{bc} = 200$  boundary points, and use them to obtain the data-driven solutions through the use of the initial and boundary conditions described above. We also generate  $N_r = 10,000$  residual points by adopting the same sampling strategy used for the previous examples. The RAR strategy is used as previously mentioned. We aim to recover the dark two-soliton solutions given by (17) and (18) by applying the enhanced PINN framework. In doing so, we use a neural network model with 4 hidden layers and 100 neurons per layer. The underlying PINN model aims to learn the hidden patterns from the training data by minimizing the loss functions corresponding to the initial and boundary conditions, the residuals of the governing equations, and the slope recovery term. After 30,000 iterations of the Adam optimizer with learning rate 0.0001 over 2132.0729 s, we continue the optimization with 5,215 iterations of the L-BFGS optimizer over 878.2534 s, and precisely simulate the dark two-soliton solutions to the system of equations (3). During this process, our model successfully reduced the  $\mathbb{L}^2$  relative errors for  $\psi_1$  and  $\psi_2$  from 0.31% and 0.32% to 0.22% and 0.25%, respectively. In Fig. 9, the density plots of the exact and predicted dynamics in the  $x-t$  and  $y-t$  planes (top row) and the  $x-y$  plane (middle row) are displayed, showing that the parallel dark two-solitons do not interact with each other. Additionally, we compare the exact and predicted solutions at different temporal levels in the bottom row of Fig. 9, which shows that our trained model successfully captured the data-driven solutions to the system of equations (3). The evolution of the predicted dynamics in the  $x-t$  plane (for  $y = 6$ ) and the  $y-t$  plane (for  $x = 8$ ), along with the corresponding point-wise errors, are displayed through three-dimensional plots in Fig. 10. The behavior of the loss functions during training with the Adam optimizer and the L-BFGS optimizer is illustrated in Fig. 11. In the left panel, the loss curves corresponding to the overall loss function, initial condition loss function, boundary condition loss function, and residual loss function are displayed, showing a slow decrease in loss values with many oscillations. The final loss values for each loss function after training with the Adam optimizer are recorded, respectively, as follows:  $2.751e-02$ ,  $2.262e-03$ ,  $8.808e-04$ , and  $1.235e-02$ . From the middle panel, one can see that the individual residual losses behave relatively close to each other. In the right panel of Fig. 11, the L-BFGS optimizer exhibits smooth behavior of the loss values during training, with the final loss values recorded as follows:  $8.103e-03$  for the overall loss function,  $2.397e-05$  for the initial condition loss,  $8.341e-05$  the boundary condition loss, and  $4.409e-03$  for the residual loss.

- Parallel cubic dark two-solitons

By taking  $\eta = 1, \sigma_1 = 1, k = 4, \mu = \lambda = 1 + i, \theta_1 = \frac{\pi}{4}, \theta_2 = \frac{\pi}{3}$ , and choosing the dispersion coefficient as  $\alpha(t) = \frac{1}{5}t^2$ , the cubic dark two-solitons to the (2+1)-dimensional VC-CNLSE (3) can be obtained. Here, the nonlinearity coefficient is considered as  $\beta(t) = -\eta\alpha(t)$ . We consider the following initial and boundary conditions for this type of soliton dynamics, with the spatial and temporal domains



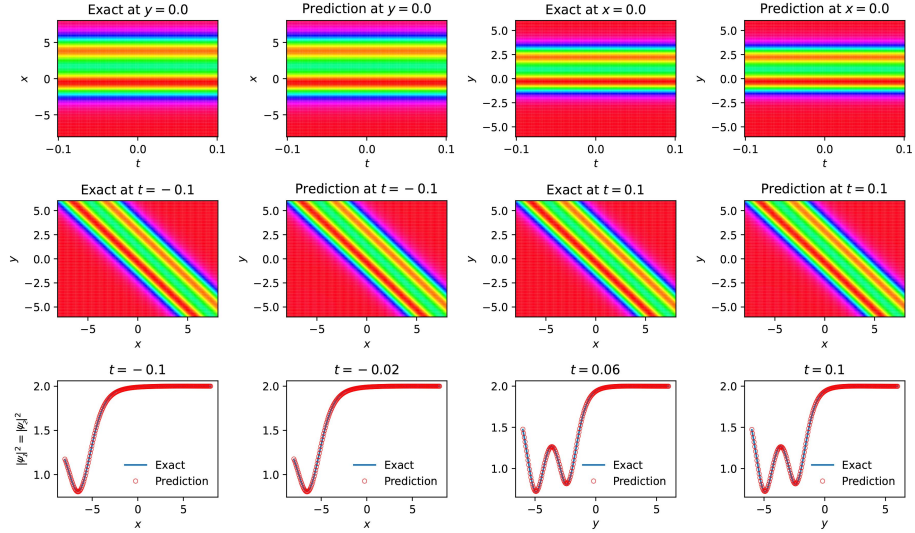


**Fig. 9** The density plots of the exact and predicted dynamics (top and middle rows) and the comparison between the exact and predicted solutions at different temporal levels (bottom row).

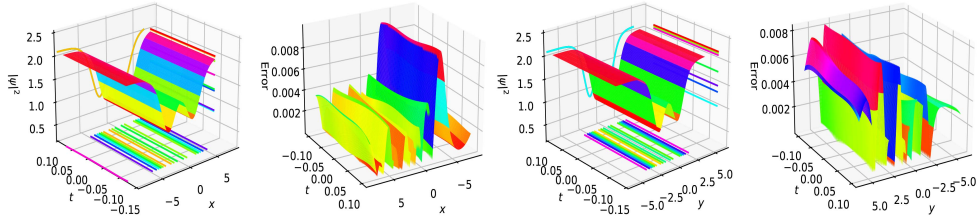


**Fig. 10** Three-dimensional plots with contour maps and the corresponding point-wise errors for  $\psi_j$  in the  $x-t$  plane (first and second panels) and  $y-t$  plane (third and fourth panels), from left to right.

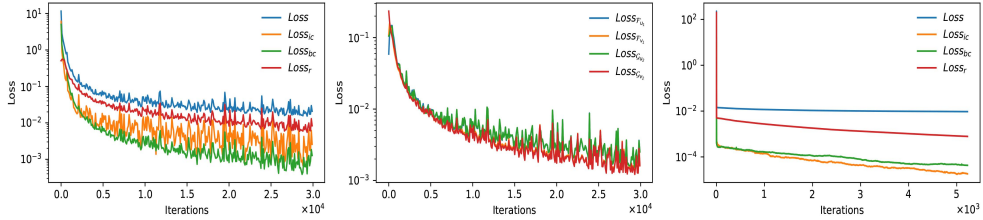


**Fig. 11** The loss curves during the training with 30,000 iterations of the Adam optimizer (left and middle panels) and the loss curves with 5,215 iterations of the L-BFGS optimizer (right panel).

defined as  $\Omega = [-10, 10] \times [-6, 6]$  and  $[-2, 2]$ , respectively. Then, for  $j = 1, 2$  we have

$$\begin{cases} \psi_j(x, y, t = -2) = \psi_j^{ic}(x, y, t = -2), & (x, y) \in \Omega, \\ \psi_j(x = -10, y, t) = \psi_j^{bc}(x = -10, y, t), & (y, t) \in [-6, 6] \times (-2, 2], \\ \psi_j(x, y = -6, t) = \psi_j^{bc}(x, y = -6, t), & (x, t) \in [-10, 10] \times (-2, 2], \\ \psi_j(x = 10, y, t) = \psi_j^{bc}(x = 10, y, t), & (y, t) \in [-6, 6] \times (-2, 2], \\ \psi_j(x, y = 6, t) = \psi_j^{bc}(x, y = 6, t), & (x, t) \in [-10, 10] \times (-2, 2], \end{cases}$$



where  $\psi_j^{ic}$  and  $\psi_j^{bc}$  can be constructed, considering the provided constant values and the dispersion and nonlinearity coefficients for the dark two-soliton solutions (17)-(23). As before, we first divide the computational domain  $\Omega \times [-2, 2]$  into  $256 \times 256$  discrete equidistant points. We set  $N_{ic} = 200$  and  $N_{bc} = 200$  corresponding to the initial and boundary training data to be randomly chosen. In order to embed the physical laws described by the governing equations into the model's knowledge, we generate  $N_r = 10,000$  residual points using the LHS strategy within the computational domain. We trained a PINN model based on the enhanced framework, equipped with a neural network model with the same structure as in the previous example. We used 30,000 iterations of the Adam optimizer and 5,034 iterations of the L-BFGS optimizer, with training times of 2135.0391 s and 870.8201 s, respectively. Our trained model achieved the  $\mathbb{L}^2$  relative errors of 0.64% and 0.65% for  $\psi_1$  and  $\psi_2$ , respectively, with the Adam optimizer, and 0.15% and 0.16% with the L-BFGS optimizer. The dynamical behaviors of the exact and predicted cubic dark two-solitons are illustrated in the  $x-t$  and  $y-t$  planes in the top row, and the  $x-y$  plane in the middle row of Fig. 12. One can see that the dark two-solitons do not interact with each other during propagation. To demonstrate that our trained model accurately captures the exact dynamics, comparisons between the predicted dynamics at different temporal levels are presented in the bottom row of Fig. 12. In Fig. 13, the evolution of the predicted dynamics in the  $x-t$  plane (for  $y = 6$ ) and the  $y-t$  plane (for  $x = 10$ ), with the corresponding point-wise errors, is displayed through three-dimensional plots. The loss values during the training phase with the Adam optimizer and L-BFGS optimizer are illustrated in Fig. 14. It can be seen that, the Adam optimizer exhibits oscillatory behavior in the loss functions during training, whereas the L-BFGS optimizer shows gradual descent without such oscillations. The loss values for the overall loss function, initial condition loss function, boundary condition loss function, and residual loss function after training with the Adam optimizer are recorded as follows:  $1.608e-02$ ,  $7.672e-05$ ,  $9.445e-05$ , and  $8.703e-04$ , respectively. Continuing the optimization process with the L-BFGS optimizer reduced these loss values to:  $6.504e-03$ ,  $2.494e-06$ ,  $4.660e-06$ , and  $5.238e-05$ , respectively. In the middle panel of Fig. 14, the behavior of the individual residual losses is depicted, showing that these loss values are relatively close to one another.

### 3.2 Data-driven parameter discovery to (2+ 1)-dimensional VC-CNLSE

In this part of the paper, we consider the data-driven parameter discovery for the (2+1)-dimensional VC-CNLSE (3). When solving the inverse problems, we do not need to make significant changes to the code used for solving the forward problems. We investigate two approaches for parameter discovery in the system of model equations (3): constant parameter discovery and variable parameter discovery.

- Data-driven constant parameter discovery

For the constant parameter discovery, we use the introduced enhanced PINN framework to predict the constant coefficient  $\tau$  through training a PINN model. Given the

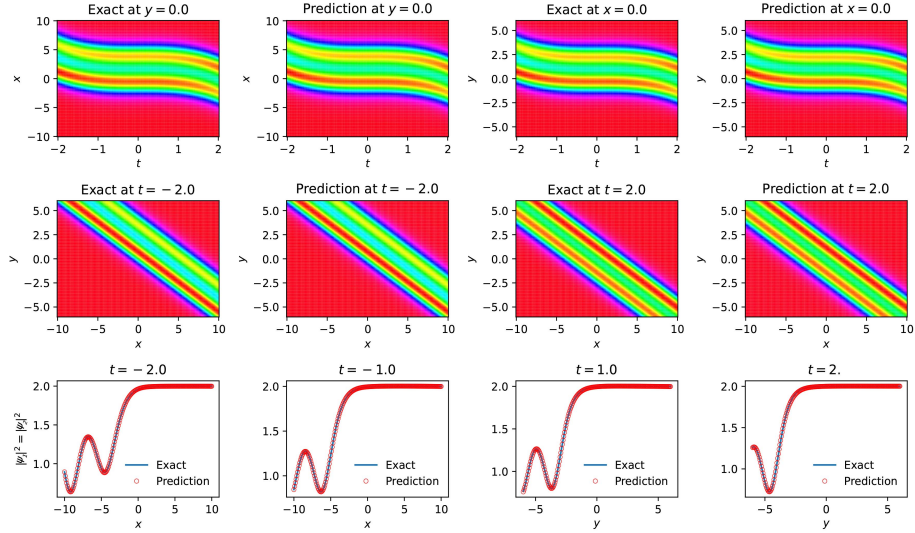


**Fig. 12** The density plots of the exact and predicted dynamics (top and middle rows) and the comparison between the exact and predicted solutions at different temporal levels (bottom row).

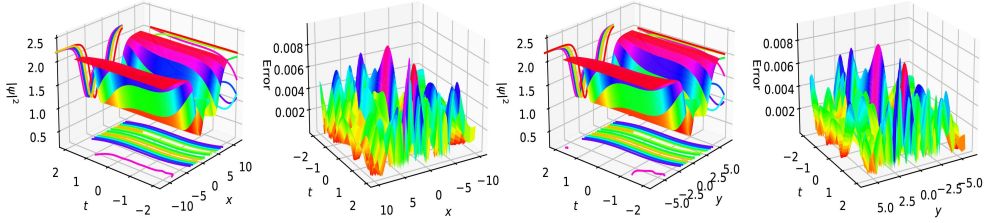


**Fig. 13** Three-dimensional plots with contour maps and the corresponding point-wise errors for  $\psi_j$  in the  $x-t$  plane (first and second panels) and  $y-t$  plane (third and fourth panels), from left to right.

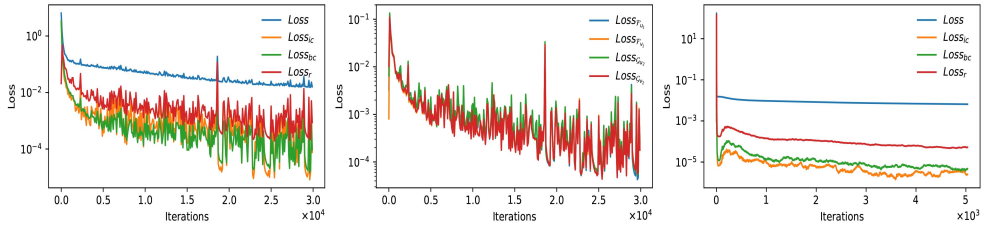


**Fig. 14** The loss curves during the training with 30,000 iterations of the Adam optimizer (left and middle panels) and the loss curves with 5,034 iterations of the L-BFGS optimizer (right panel).

same parameters for the parabolic vector dark one-soliton, we discretize the spatial and temporal domains into  $256 \times 256 \times 201$  equidistant points. We randomly sample  $N_o = 1,000$  points from the generated data, then create a set of observations of

the exact solutions  $\left\{u_1^k, v_1^k, u_2^k, v_2^k\right\}_{k=1}^{N_o}$  based on the sampled data points. The data-driven parameter discovery to predict the constant coefficient  $\tau$  will be performed by training an enhanced PINN model, which is equipped with a neural network containing 5 hidden layers with 40 neurons per layer, through an optimization process that minimizes the following loss function:

$$\begin{aligned} Loss(\boldsymbol{\theta}) := & \frac{1}{N_o} \sum_{k=1}^{N_o} \left( \left| u_1^k - \hat{u}_{1,\boldsymbol{\theta}}(\mathbf{X}^k, t^k) \right|^2 + \left| v_1^k - \hat{v}_{1,\boldsymbol{\theta}}(\mathbf{X}^k, t^k) \right|^2 \right. \\ & + \left. \left| u_2^k - \hat{u}_{2,\boldsymbol{\theta}}(\mathbf{X}^k, t^k) \right|^2 + \left| v_2^k - \hat{v}_{2,\boldsymbol{\theta}}(\mathbf{X}^k, t^k) \right|^2 \right) \\ & + \frac{1}{N_r} \sum_{j=1}^{N_r} w_r^{(k)} \left( \left| \mathcal{F}_{\hat{u}_{1,\boldsymbol{\theta}}}(\mathbf{X}^j, t^j) \right|^2 + \left| \mathcal{F}_{\hat{v}_{1,\boldsymbol{\theta}}}(\mathbf{X}^j, t^j) \right|^2 \right. \\ & + \left. \left| \mathcal{G}_{\hat{u}_{2,\boldsymbol{\theta}}}(\mathbf{X}^j, t^j) \right|^2 + \left| \mathcal{G}_{\hat{v}_{2,\boldsymbol{\theta}}}(\mathbf{X}^j, t^j) \right|^2 \right) + \frac{w_a}{\frac{1}{D-1} \sum_{\ell=1}^{D-1} \exp\left(\frac{\sum_{k=1}^{N^\ell} a_k^\ell}{N^\ell}\right)}, \end{aligned}$$

where  $\boldsymbol{\theta}$  represents the set of all trainable parameters, including the weights, biases, scalable parameters, and the parameter  $\hat{\tau}$ , which serves as a prediction of the true value of  $\tau$ . We initialized this trainable parameter as  $\hat{\tau} = 0$ . Minimizing this loss function allows our PINN model to align its predictions with data-driven observations while embedding the physical laws into the model's knowledge. Incorporating these physical laws into the training phase is the key feature of the PINN model to predict the true value of the constant coefficient  $\tau$ . We allow our model to learn the true value of the constant coefficient  $\tau$  by treating this parameter as one of the trainable parameters within the underlying neural network model. We used 10,000 iterations of the Adam optimizer with the default learning rate, followed by a run of the L-BFGS optimizer, to obtain the optimal values of the trainable parameters. During this process, the  $\mathbb{L}^2$  relative error between the true value of  $\tau$  and its prediction  $\hat{\tau}$  decreased from 0.61% to 0.013%, demonstrating that our trained model can predict the true value of  $\tau$  with high accuracy. To evaluate the performance of the enhanced PINN model for data-driven parameter discovery in the (2+ 1)-dimensional VC-CNLSE under noisy conditions, we introduce different noise intensities to the observational data. For a fair comparison, we use the same initialization for all networks trained with different noise intensities. As reported in Table 1, the enhanced PINN model accurately predicts the true value of the constant coefficient  $\tau$  even when the observational data is corrupted with noise. It is evident that increasing noise levels leads to higher prediction errors and negatively impacts loss convergence. The left panel of Fig. 15 depicts the process of our PINN model learning the true value of the constant coefficient  $\tau$ . During the iterations of the Adam optimizer (solid lines), followed by the L-BFGS optimizer (dashed lines), our PINN model gradually predicts the true value of  $\tau$  with high accuracy. One can see that increasing the noise levels will have a negative impact on the predictions. Training under different noise intensities alters the loss values, as shown in the middle panel of Fig. 15. The  $\mathbb{L}^2$  relative errors between the constant coefficient  $\tau$  and

its prediction  $\hat{\tau}$  for different levels of added noise are illustrated in the right panel of Fig. 15. It can be seen that as the noise level increases from 0 to 15, the relative error also increases, and continuing the optimization with the L-BFGS optimizer does not have a significant effect on prediction accuracy. In Table 2, we investigate the effect of the number of observations on the prediction accuracy through the lens of  $\mathbb{L}^2$  relative error. It can be seen that increasing the number of observations reduces the relative error, even in the presence of noisy data. In summary, our enhanced PINN model achieves lower prediction error and faster convergence with clean data (noise = 0%). However, introducing noise into the data negatively impacts the model's prediction accuracy and convergence.

**Table 1** The  $\mathbb{L}^2$  relative errors and loss values of the discovered coefficient under noise intensities (Adam+L-BFGS).

Noise (%)	Predicted values of $\tau$	$\mathbb{L}^2$ relative errors (%)	Loss values
0	0.9998723	0.013	$8.536e-03$
5	0.9984364	0.16	$1.934e-02$
10	0.98912466	1.09	$4.896e-02$
15	1.01243	1.24	$1.042e-01$

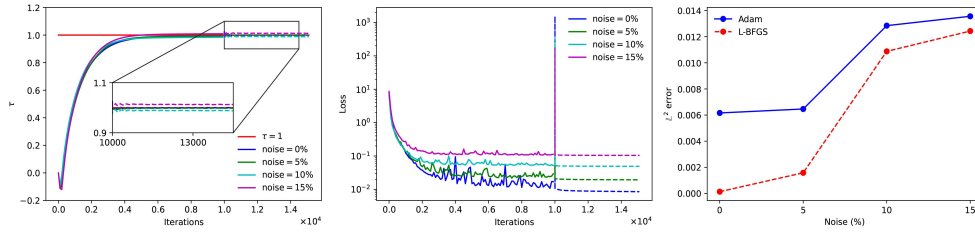


**Fig. 15** The predictions of the constant coefficient  $\tau$  (left panel), the behavior of the loss functions Adam + L-BFGS (middle panel), and the prediction errors (right panel) under different noise intensities.

**Table 2** The  $\mathbb{L}^2$  relative errors of  $\tau$  under noise intensities and varying  $N_o$  (Adam + L-BFGS).

Data type	$\mathbb{L}^2$ relative errors (%)			
	$N_o = 100$	500	1000	1500
Clean data (0%)	0.045	0.0027	0.013	0.0013
Noisy data (5%)	1.57	0.45	0.056	0.11
Noisy data (10%)	0.27	1.01	1.09	0.38
Noisy data (15%)	11.93	1.20	1.24	0.17

- Data-driven variable parameter discovery

Here, we investigate the capability of the proposed enhanced PINN framework in capturing the dynamic behavior of the variable dispersion and nonlinearity coefficients  $\alpha(t)$  and  $\beta(t)$  for the (2+ 1)-dimensional VC-CNLSE (3). In doing so, we employ a dual-network strategy for the enhanced PINN algorithm, where one network is responsible for predicting the solutions  $\psi_1$  and  $\psi_2$ , while another network is tasked with predicting the dynamic behavior of the variable coefficients. Incorporating the physical laws described by the system of equations (3) into the training phase is the key feature of the enhanced PINN framework, enabling the model to learn the dynamic behavior of the variable coefficients with a small amount of training data. We consider the same parameter configuration as for the vector m-shaped anti-dark one-soliton solution and train a PINN model based on the enhanced framework to predict the dynamic behavior of the following dispersion and nonlinearity coefficients:

$$\alpha(t) = t \ln(t^2), \quad \beta(t) = -\frac{\csc^2(\theta)(k^2 + m^2)t \ln(t^2)}{2(|\lambda|^2 + |\mu|^2)}.$$

Since these coefficients are functions of the temporal variable  $t$ , the corresponding neural network should process the temporal coordinate as input data to learn the dynamic of these coefficients. We divide the computational domain  $\Omega \times [-2, 2]$  into  $256 \times 256 \times 200$  discrete equidistant points and randomly sample  $N_o = 2,000$  data observations from the generated data points. We also sample  $N_r = 20,000$  residual points using the LHS strategy within the computational domain. Additionally, we divide the temporal domain  $[-2, 2]$  into 1,000 equidistant points to assess the accuracy of the underlying PINN model in predicting the variable coefficients through the lens of the  $\mathbb{L}^2$  relative error. Our PINN model will be equipped with a neural network parameterized by  $\boldsymbol{\theta}_1$ , using spatial and temporal coordinates as input data to train and predict the solutions  $\psi_1$  and  $\psi_2$ , along with another network parameterized by  $\boldsymbol{\theta}_2$ , which takes only the temporal coordinate as input data to predict the variable coefficients. Both networks may or may not have the same hidden layer structure and will be trained simultaneously. In this experiment, the first network has 5 hidden layers with 40 neurons in each, while the second network has 3 hidden layers with 30 neurons per layer. We consider the locally adaptive activation tanh function for both networks to accelerate the convergence speed. Then, the underlying PINN model aims to learn the dynamic behavior of both the solutions  $\psi_1$  and  $\psi_2$ , as well as the dynamic behavior of the variable coefficients, through a minimization problem by minimizing the following loss function:

$$\begin{aligned} Loss(\boldsymbol{\theta}_1, \boldsymbol{\theta}_2) := & \frac{1}{N_o} \sum_{k=1}^{N_o} \left( \left| u_1^k - \hat{u}_{1,\boldsymbol{\theta}_1}(\mathbf{X}^k, t^k) \right|^2 + \left| v_1^k - \hat{v}_{1,\boldsymbol{\theta}_1}(\mathbf{X}^k, t^k) \right|^2 \right. \\ & \left. + \left| u_2^k - \hat{u}_{2,\boldsymbol{\theta}_1}(\mathbf{X}^k, t^k) \right|^2 + \left| v_2^k - \hat{v}_{2,\boldsymbol{\theta}_1}(\mathbf{X}^k, t^k) \right|^2 \right) \\ & + \frac{1}{N_r} \sum_{j=1}^{N_r} w_r^{(k)} \left( \left| \mathcal{F}_{\hat{u}_{1,\boldsymbol{\theta}_1,\boldsymbol{\theta}_2}}(\mathbf{X}^j, t^j) \right|^2 + \left| \mathcal{F}_{\hat{v}_{1,\boldsymbol{\theta}_1,\boldsymbol{\theta}_2}}(\mathbf{X}^j, t^j) \right|^2 \right) \end{aligned}$$

$$\begin{aligned}
& + \left| \mathcal{G}_{\hat{u}_2, \theta_1, \theta_2}(\mathbf{X}^j, t^j) \right|^2 + \left| \mathcal{G}_{\hat{v}_2, \theta_1, \theta_2}(\mathbf{X}^j, t^j) \right|^2 \\
& + Loss_{a_1} + Loss_{a_2},
\end{aligned}$$

where  $\theta_1$  and  $\theta_2$  are the sets of trainable parameters for the first network, which outputs the real and imaginary parts of the decomposed solutions  $\psi_1$  and  $\psi_2$ , and the second network, which outputs the predictions of the variable coefficients, respectively.  $Loss_{a_1}$  and  $Loss_{a_2}$  denote the slope recovery loss terms for the first and second networks, respectively. After 10,000 iterations of the Adam optimizer and some iterations of the L-BFGS optimizer with clean data (noise = 0%), the  $\mathbb{L}^2$  relative error of the variable coefficients  $\alpha(t)$  and  $\beta(t)$  decreased from 0.40% to 0.28% and 0.65% to 0.45%, respectively. When we add noise levels of 5%, 10%, and 15% into the training observations, the  $\mathbb{L}^2$  relative error of the dispersion coefficient  $\alpha(t)$  changes from 0.53%, 0.55%, and 0.57% to 0.33%, 0.27%, and 0.33%, respectively, when we first use iterations of the Adam optimizer and then continue the optimization process with the L-BFGS optimizer. This scenario holds for the nonlinearity coefficient  $\beta(t)$ , where the  $\mathbb{L}^2$  relative error changes from 0.61%, 0.67%, and 0.72% to 0.42%, 0.40%, and 0.60%, when we add noise levels of 5%, 10%, and 15% into the training observations, respectively. The predictions of the dispersion and nonlinearity coefficients  $\alpha(t)$  and  $\beta(t)$  under different noise levels are displayed in the left and middle panels of Fig. 16. One can see that our enhanced trained PINN model can accurately predict the dynamic behavior of both variable coefficients, even in the presence of noise intensities. The  $\mathbb{L}^2$  relative errors of both the dispersion and nonlinearity variable coefficients  $\alpha(t)$  and  $\beta(t)$  for different noise intensities are illustrated in the right panel of Fig. 16, which shows that increasing the noise levels does not significantly impact prediction accuracy. The obtained results show that our enhanced PINN model can accurately predict the behavior of the variable coefficients  $\alpha(t)$  and  $\beta(t)$  in the system of model equations (3) with a small amount of training data. It should be noted that these coefficients are nonlinear functions of the temporal variable. These results confirm that the proposed algorithm is robust even when noise levels are added to the training observations. In summary, the proposed enhanced PINN framework introduces a promising modeling approach in the field of optical fiber communication by accurately capturing the dynamic behavior of variable coefficients in nonlinear systems. Its robustness against noisy data makes it a reliable tool for real world applications, where measurement uncertainties are common. The ability to maintain high prediction accuracy under different noise intensities highlights the potential of this framework for parameter discovery and system identification in complex, data-driven environments.

## 4 Conclusions

In this study, we proposed an enhanced PINN framework for data-driven soliton solutions and parameter discovery to the (2+ 1)-dimensional VC-CNLSE. We introduced a locally adaptive activation function to our PINN algorithm to accelerate the convergence speed of the training process. PINN algorithms enhance the capabilities of neural networks by incorporating the physical knowledge, described by differential

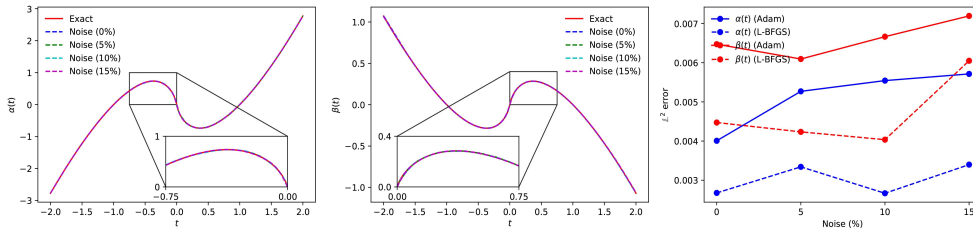


**Fig. 16** The predictions of the dispersion coefficient  $\alpha(t)$  (left panel) and the nonlinearity coefficient  $\beta(t)$  (middle panel) and the related prediction errors (right panel) under different noise intensities.

equations, into the training phase. Incorporating physical knowledge into the training phase allows the network to learn from both data and the underlying principles governing the problem, leading to more accurate and physically consistent predictions. By leveraging the residual-based adaptive refinement (RAR) strategy, we introduced a region-specific weighted loss function, demonstrating that different distributions of physical knowledge are required when training a PINN model for the  $(2+1)$ -dimensional VC-CNLSE. We demonstrated the framework's effectiveness in capturing the dynamics of vector dark and anti-dark one- and two-soliton structures through various soliton solutions and the corresponding data-driven predictions. The density plots of the exact and predicted solutions are displayed, and the related evolution dynamics are illustrated through three-dimensional plots. We also compared the exact and predicted solutions at different temporal levels to show the accuracy of the trained model's prediction. We performed data-driven parameter discovery for the  $(2+1)$ -dimensional VC-CNLSE, categorizing it into two classes: constant parameter discovery and variable parameter discovery. For constant parameter discovery, we employed an enhanced PINN model equipped with a single neural network to estimate the value of the constant parameter in the system of model equations. For variable parameter discovery, we used a dual-network strategy within the proposed PINN framework to capture the dynamic behavior of the variable dispersion and nonlinearity coefficients. As these coefficients are nonlinear functions of the temporal variable, this shows that our enhanced PINN framework is capable of capturing complex nonlinear variable coefficients. This robustness highlights the framework's potential for broader applications in complex optical fiber systems. The obtained results confirm that the proposed enhanced PINN framework offers a powerful and versatile approach for solving high-dimensional, complex solitonic dynamics in optical communication systems. Its robustness, accuracy, and adaptability make it a promising tool for advancing research and applications in nonlinear optics and related fields.

## References

- [1] Kudryashov, N.A.: Construction of nonlinear differential equations for description of propagation pulses in optical fiber. *Optic.* **192**, 162964 (2019) <https://doi.org/10.1016/j.ijleo.2019.162964>
- [2] Ibrahim, S., Baleanu, D.: Classes of solitary solution for nonlinear schrödinger



- equation arising in optical fibers and their stability analysis. *Opt. Quant. Electron.* **55**, 1158 (2023) <https://doi.org/10.1007/s11082-023-05423-2>
- [3] Seadawy, A.R., Cheemaa, N.: Propagation of nonlinear complex waves for the coupled nonlinear schrödinger equations in two core optical fibers. *Phys. A Stat. Mech. Appl.* **529**, 121330 (2019) <https://doi.org/10.1016/j.physa.2019.121330>
- [4] Li, M., Xu, T., Wang, L.: Dynamical behaviors and soliton solutions of a generalized higher-order nonlinear schrödinger equation in optical fibers. *Nonlinear Dyn.* **80**, 1451–1461 (2015) <https://doi.org/10.1007/s11071-015-1954-z>
- [5] Chabchoub, A., Kibler, B., Finot, C., Millot, G., Onorato, M., Dudley, J.M., Babanin, A.V.: The nonlinear schrödinger equation and the propagation of weakly nonlinear waves in optical fibers and on the water surface. *Ann. Nucl. Energy* **361**, 490–500 (2015) <https://doi.org/10.1016/j.aop.2015.07.003>
- [6] Pankratova, M., Vasylychenkova, A., Derevyanko, S.A., Chichkov, N.B., Prilepsky, J.E.: Signal-noise interaction in optical-fiber communication systems employing nonlinear frequency-division multiplexing. *Phys. Rev. Appl.* **13**(12), 054021 (2020) <https://doi.org/10.1103/PhysRevApplied.13.054021>
- [7] Yang, D.Y., Tian, B., Tian, H.Y., Wei, C.C., Shan, W.R., Jiang, Y.: Darboux transformation, localized waves and conservation laws for an m-coupled variable-coefficient nonlinear schrödinger system in an inhomogeneous optical fiber. *Chaos Solitons Fractals* **156**, 111719 (2022) <https://doi.org/10.1016/j.chaos.2021.111719>
- [8] Chen, S.S., Tian, B., Chai, J., Wu, X.Y., Du, Z.: Lax pair, binary darboux transformations and dark-soliton interaction of a fifth-order defocusing nonlinear schrödinger equation for the attosecond pulses in the optical fiber communication. *Wave. Random Complex* **30**(3), 389–402 (2020) <https://doi.org/10.1080/17455030.2018.1516053>
- [9] Ma, G., Zhao, J., Zhou, Q., Biswas, A., Liu, W.: Soliton interaction control through dispersion and nonlinear effects for the fifth-order nonlinear schrödinger equation. *Nonlinear Dyn.* **106**, 2479–2484 (2021) <https://doi.org/10.1007/s11071-021-06915-0>
- [10] Wazwaz, A.M.: Bright and dark optical solitons of the (2+ 1)-dimensional perturbed nonlinear schrödinger equation in nonlinear optical fibers. *Optik* **251**, 168334 (2022) <https://doi.org/10.1016/j.ijleo.2021.168334>
- [11] Xu, T., Shevchenko, N.A., Zhang, Y., Jin, C., Zhao, J., Liu, T.: Information rates in kerr nonlinearity limited optical fiber communication systems. *Opt. Express* **29**(11), 17428–17439 (2021) <https://doi.org/10.1364/OE.415753>
- [12] Tozar, A., Tasbozan, O., Kurt, A.: Optical soliton solutions for

- the  $(1+1)$ -dimensional resonant nonlinear schrödinger's equation arising in optical fibers. *Opt. Quant. Electron.* **53**(6), 316 (2021) <https://doi.org/10.1007/s11082-021-02913-z>
- [13] Li, Z., Huang, C., Wang, B.: Phase portrait, bifurcation, chaotic pattern and optical soliton solutions of the fokas-lenells equation with cubic-quartic dispersion in optical fibers. *Phys. Lett. A* **465**, 128714 (2023) <https://doi.org/10.1016/j.physleta.2023.128714>
- [14] Tang, L.: Bifurcations and optical solitons for the coupled nonlinear schrödinger equation in optical fiber bragg gratings. *J. Opt.* **52**(3), 1388–1398 (2023) <https://doi.org/10.1007/s12596-022-00963-4>
- [15] Ahmad, J., Akram, S., Noor, K., Nadeem, M., Bucur, A., Alsayaad, Y.: Soliton solutions of fractional extended nonlinear schrödinger equation arising in plasma physics and nonlinear optical fiber. *Sci. Rep.* **13**(1), 10877 (2023) <https://doi.org/10.1038/s41598-023-37757-y>
- [16] Copie, F., Randoux, S., Suret, P.: The physics of the one-dimensional nonlinear schrödinger equation in fiber optics: Rogue waves, modulation instability and self-focusing phenomena. *Rev. Phys.* **5**, 100037 (2020) <https://doi.org/10.1016/j.revip.2019.100037>
- [17] Ibrahim, S., Ashir, A.M., Sabawi, Y.A., Baleanu, D.: Realization of optical solitons from nonlinear schrödinger equation using modified sardar sub-equation technique. *Opt. Quant. Electron.* **55**(7), 617 (2023) <https://doi.org/10.1007/s11082-023-04776-y>
- [18] Meng, Z., Yang, Y.: Quantum computing of fluid dynamics using the hydrodynamic schrödinger equation. *Phys. Rev. Res.* **5**(3), 033182 (2023) <https://doi.org/10.1103/PhysRevResearch.5.033182>
- [19] Islam, M.T., Akbar, M.A., Guner, O., Bekir, A.: Apposite solutions to fractional nonlinear schrödinger-type evolution equations occurring in quantum mechanics. *Mod. Phys. Lett. B.* **35**(30), 2150470 (2021) <https://doi.org/10.1142/S0217984921504704>
- [20] Te Vrugt, M., Frohoff-Hülsmann, T., Heifetz, E., Thiele, U., Wittkowski, R.: From a microscopic inertial active matter model to the schrödinger equation. *Nat. Commun.* **14**(1), 1302 (2023) <https://doi.org/10.1038/s41467-022-35635-1>
- [21] Ahmad, J., Akram, S., Noor, K., Nadeem, M., Bucur, A., Alsayaad, Y.: Soliton solutions of fractional extended nonlinear schrödinger equation arising in plasma physics and nonlinear optical fiber. *Sci. Rep.* **13**(1), 10877 (2023) <https://doi.org/10.1038/s41598-023-37757-y>
- [22] Salas, A.H., El-Tantawy, S.A., Castillo H, J.E.: The hybrid finite difference and

- moving boundary methods for solving a linear damped nonlinear schrödinger equation to model rogue waves and breathers in plasma physics. *Math. Probl. Eng.* **2020**(1), 6874870 (2020) <https://doi.org/10.1155/2020/6874870>
- [23] Boulaaras, S.M., Rehman, H.U., Iqbal, I., Sallah, M., Qayyum, A.: Unveiling optical solitons: Solving two forms of nonlinear schrödinger equations with unified solver method. *Optic* **295**, 171535 (2023) <https://doi.org/10.1016/j.ijleo.2023.171535>
- [24] Farag, N.G., Eltanboly, A.H., El-Azab, M.S., Obayya, S.S.A.: On the analytical and numerical solutions of the one-dimensional nonlinear schrodinger equation. *Optic* **2021**(1), 3094011 (2021) <https://doi.org/10.1016/j.ijleo.2023.171535>
- [25] Yu, W., Liu, W., Triki, H., Zhou, Q., Biswas, A., Belić, M.R.: Control of dark and anti-dark solitons in the  $(2+1)$ -dimensional coupled nonlinear schrödinger equations with perturbed dispersion and nonlinearity in a nonlinear optical system. *Nonlinear Dyn.* **97**, 471–483 (2019) <https://doi.org/10.1007/s11071-019-04992-w>
- [26] Gürses, M., Pekcan, A.: Nonlocal nonlinear schrödinger equations and their soliton solutions. *J. Math. Phys.* **59**(5), 051501 (2018) <https://doi.org/10.1063/1.4997835>
- [27] Ablowitz, M.J., Musslimani, Z.H.: Inverse scattering transform for the integrable nonlocal nonlinear schrödinger equation. *Nonlinearity* **29**(3), 915 (2016) <https://doi.org/10.1063/1.4997835>
- [28] Biondini, G., Kovačič, G.: Inverse scattering transform for the focusing nonlinear schrödinger equation with nonzero boundary conditions. *J. Math. Phys.* **55**(3), 031506 (2014) <https://doi.org/10.1063/1.4868483>
- [29] Barletti, L., Brugnano, L., Caccia, G.F., Iavernaro, F.: Energy-conserving methods for the nonlinear schrödinger equation. *Appl. Math. Comput.* **318**, 3–18 (2018) <https://doi.org/10.1016/j.amc.2017.04.018>
- [30] Arora, G., Joshi, V., Mittal, R.C.: Numerical simulation of nonlinear schrödinger equation in one and two dimensions. *Math. Models Comput. Simul.* **11**, 634–648 (2019) <https://doi.org/10.1134/S2070048219040070>
- [31] Kaup, D.J., Newell, A.C.: An exact solution for a derivative nonlinear schrödinger equation. *J. Math. Phys.* **19**(4), 798–801 (1978)
- [32] Hayashi, N., Ozawa, T.: On the derivative nonlinear schrödinger equation. *Physica D.* **55**(1–2), 14–36 (1992) [https://doi.org/10.1016/0167-2789\(92\)90185-P](https://doi.org/10.1016/0167-2789(92)90185-P)
- [33] Kohl, R.W., Biswas, A., Ekici, M., Zhou, Q., Khan, S., Alshomrani, A.S., Belić, M.R.: Highly dispersive optical soliton perturbation with

- kerr law by semi-inverse variational principle. *Optic* **199**, 163226 (2019) <https://doi.org/10.1016/j.ijleo.2019.163226>
- [34] Ablowitz, M.J., Musslimani, Z.H.: Integrable nonlocal nonlinear schrödinger equation. *Phys. Rev. Lett.* **110**(6), 064105 (2013) <https://doi.org/10.1103/PhysRevLett.110.064105>
- [35] Zhang, Y., Yang, C., Yu, W., Mirzazadeh, M., Zhou, Q., Liu, W.: Interactions of vector anti-dark solitons for the coupled nonlinear schrödinger equation in inhomogeneous fibers. *Nonlinear Dyn.* **94**, 1351–1360 (2018) <https://doi.org/10.1007/s11071-018-4428-2>
- [36] Abdelrahman, M.A., Hassan, S.Z., Inc, M.: The coupled nonlinear schrödinger-type equations. *Mod. Phys. Lett. B.* **34**(6), 2050078 (2020) <https://doi.org/10.1142/S0217984920500785>
- [37] Kevrekidis, P.G., Frantzeskakis, D.J.: Solitons in coupled nonlinear schrödinger models: a survey of recent developments. *Rev. Phys.* **1**, 140–153 (2016) <https://doi.org/10.1016/j.revip.2016.07.002>
- [38] Kivshar, Y.S., Agrawal, G.P. (eds.): *Optical Solitons: from Fibers to Photonic Crystals*. Academic Press, ??? (2013)
- [39] Kanna, T., Lakshmanan, M., Dinda, P.T., Akhmediev, N.: Soliton collisions with shape change by intensity redistribution in mixed coupled nonlinear schrödinger equations. *Phys. Rev. E.* **73**(2), 026604 (2006) <https://doi.org/10.1103/PhysRevE.73.026604>
- [40] Ohta, Y., Wang, D.S., Yang, J.: General n-dark–dark solitons in the coupled nonlinear schrödinger equations. *Stud. Appl. Math.* **127**(4), 345–371 (2011) <https://doi.org/10.1111/j.1467-9590.2011.00525.x>
- [41] Zhang, G., Yan, Z., Wen, X.Y., Chen, Y.: Interactions of localized wave structures and dynamics in the defocusing coupled nonlinear schrödinger equations. *Phys. Rev. E.* **95**(4), 042201 (2017) <https://doi.org/10.1103/PhysRevE.95.042201>
- [42] Wang, L., Luan, Z., Zhou, Q., Biswas, A., Alzahrani, A.K., Liu, W.: Bright soliton solutions of the (2+ 1)-dimensional generalized coupled nonlinear schrödinger equation with the four-wave mixing term. *Nonlinear Dyn.* **104**, 2613–2620 (2021) <https://doi.org/10.1007/s11071-021-06411-5>
- [43] Yang, L., Gao, B.: Solitons, kink-solitons and breather solutions of the two-coupled incoherent nonlinear schrödinger equation. *Nonlinear Dyn.* **112**(7), 5621–5633 (2024) <https://doi.org/10.1007/s11071-024-09336-x>
- [44] Lan, Z.Z., Gao, B., Du, M.J.: Dark solitons behaviors for a (2+ 1)-dimensional coupled nonlinear schrödinger system in an optical fiber. *Chaos Solitons Fractals*

111, 169–174 (2018) <https://doi.org/10.1016/j.chaos.2018.04.005>

- [45] Xu, T., Li, H., Zhang, H., Li, M., Lan, S.: Darboux transformation and analytic solutions of the discrete  $pt$ -symmetric nonlocal nonlinear schrödinger equation. *Appl. Math. Lett.* **63**, 88–94 (2017) <https://doi.org/10.1016/j.aml.2016.07.024>
- [46] Skarka, V., Berezhiani, V.I., Miklaszewski, R.: Spatiotemporal soliton propagation in saturating nonlinear optical media. *Phys. Rev. E.* **56**(1), 1080 (1997) <https://doi.org/10.1103/PhysRevE.56.1080>
- [47] Song, Y., Shi, X., Wu, C., Tang, D., Zhang, H.: Recent progress of study on optical solitons in fiber lasers. *Appl. Phys. Rev.* **6**(2) (2019) <https://doi.org/10.1063/1.5091811>
- [48] Younis, M., Cheemaa, N., Mehmood, S.A., Rizvi, S.T.R., Bekir, A.: A variety of exact solutions to  $(2+1)$ -dimensional schrödinger equation. *Waves Random Compl.* **30**(3), 490–499 (2020) <https://doi.org/10.1080/17455030.2018.1532131>
- [49] Xie, X.Y., Tian, B., Sun, W.R., Sun, Y.: Bright solitons for the  $(2+1)$ -dimensional coupled nonlinear schrödinger equations in a graded-index waveguide. *Commun. Nonlinear Sci. Numer. Simul.* **29**(1-3), 300–306 (2015) <https://doi.org/10.1016/j.cnsns.2015.05.009>
- [50] Islam, M.T., Akbar, M.A., Ahmad, H.: Diverse optical soliton solutions of the fractional coupled  $(2+1)$ -dimensional nonlinear schrödinger equations. *Opt. Quantum Electron.* **54**(2), 129 (2022) <https://doi.org/10.1007/s11082-021-03472-z>
- [51] Seadawy, A.R., Cheemaa, N., Biswas, A.: Bright soliton solutions of the  $(2+1)$ -dimensional generalized coupled nonlinear schrödinger equation with the four-wave mixing term. *Optic* **227**, 165669 (2021) <https://doi.org/10.1016/j.ijleo.2020.165669>
- [52] Das, N., Saha Ray, S.: Dispersive optical soliton solutions of the  $(2+1)$ -dimensional cascaded system governing by coupled nonlinear schrödinger equation with kerr law nonlinearity in plasma. *Optic* **55**(4), 328 (2023) <https://doi.org/10.1007/s11082-022-04285-4>
- [53] Han, L., Huang, Y., Liu, H.: Solitons in coupled nonlinear schrödinger equations with variable coefficients. *Commun. Nonlinear Sci. Numer. Simul.* **19**(9), 3063–3073 (2014) <https://doi.org/10.1016/j.cnsns.2014.01.017>
- [54] Deng, G.F., Gao, Y.T.: Solitons for the  $(3+1)$ -dimensional variable-coefficient coupled nonlinear schrödinger equations in an optical fiber. *Commun. Nonlinear Sci. Numer. Simul.* **109**, 345–359 (2017) <https://doi.org/10.1016/j.spmi.2017.02.056>
- [55] Han, Y., Tian, B., Yuan, Y.Q., Zhang, C.R., Chen, S.S.: Bilinear forms and

- bright-dark solitons for a coupled nonlinear schrödinger system with variable coefficients in an inhomogeneous optical fiber. *Chi. J. Phys.* **62**, 202–212 (2019) <https://doi.org/10.1016/j.cjph.2019.09.022>
- [56] Yang, C., Liu, W., Zhou, Q., Mihalache, D., Malomed, B.A.: One-soliton shaping and two-soliton interaction in the fifth-order variable-coefficient nonlinear schrödinger equation. *Nonlinear Dyn.* **95**, 369–380 (2019) <https://doi.org/10.1007/s11071-018-4569-3>
- [57] Su, J.J., Gao, Y.T.: Dark solitons for a  $(2+1)$ -dimensional coupled nonlinear schrödinger system with time-dependent coefficients in an optical fiber. *Superlattices Microstruct.* **104**, 498–508 (2017) <https://doi.org/10.1016/j.spmi.2016.12.056>
- [58] Yu, W., Liu, W., Triki, H., Zhou, Q., Biswas, A., Belić, M.R.: Control of dark and anti-dark solitons in the  $(2+1)$ -dimensional coupled nonlinear schrödinger equations with perturbed dispersion and nonlinearity in a nonlinear optical system. *Nonlinear Dyn.* **97**, 471–483 (2019) <https://doi.org/10.1007/s11071-019-04992-w>
- [59] Wang, X., Gao, B.: New solitons and breather-like solutions to a  $(2+1)$ -dimensional coupled variable-coefficient schrödinger equation in optical fibers. *Nonlinear Dyn.* **112**, 17321–17343 (2024) <https://doi.org/10.1007/s11071-024-09910-3>
- [60] Nadkarni, P.M., Ohno-Machado, L., Chapman, W.W.: Natural language processing: an introduction. *J. Am. Med. Inform. Assoc.* **18**(5), 544–551 (2011) <https://doi.org/10.1136/amiajnl-2011-000464>
- [61] Wäldchen, J., Mäder, P.: Machine learning for image based species identification. *Methods Ecol. Evol.* **9**(11), 2216–2225 (2018) <https://doi.org/10.1111/2041-210X.13075>
- [62] Cao, Y., Geddes, T.A., Yang, J.Y.H., Yang, P.: Ensemble deep learning in bioinformatics. *Nat. Mach. Intell.* **2**(9), 500–508 (2020) <https://doi.org/10.1038/s42256-020-0217-y>
- [63] Walker, A.S., Clardy, J.: A machine learning bioinformatics method to predict biological activity from biosynthetic gene clusters. *J. Chem. Inf. Model.* **61**(6), 2560–2571 (2021) <https://doi.org/10.1021/acs.jcim.0c01304>
- [64] O’Gorman, P.A., Dwyer, J.G.: Using machine learning to parameterize moist convection: Potential for modeling of climate, climate change, and extreme events. *J. Chem. Inf. Model.* **10**(10), 2548–2563 (2018) <https://doi.org/10.1029/2018MS001351>

- [65] Kamilaris, A., Prenafeta-Boldú, F.X.: Deep learning in agriculture: A survey. *Comput. Electron. Agric.* **147**, 70–90 (2018) <https://doi.org/10.1016/j.compag.2018.02.016>
- [66] Janiesch, C., Zschech, P., Heinrich, K.: Machine learning and deep learning. *Electron. Markets* **31**(3), 685–695 (2021) <https://doi.org/10.1007/s12525-021-00475-2>
- [67] Raissi, M., Perdikaris, P., Karniadakis, G.E.: Physics-informed neural networks: A deep learning framework for solving forward and inverse problems involving nonlinear partial differential equations. *J. Comput. Phys.* **378**, 686–707 (2019) <https://doi.org/10.1016/j.jcp.2018.10.045>
- [68] Baydin, A.G., Pearlmutter, B.A., Radul, A.A., Siskind, J.M.: Automatic differentiation in machine learning: a survey. *J. Mach. Learn. Res.* **18**(153), 1–43 (2018)
- [69] Cuomo, S., Di Cola, V.S., Giampaolo, F., Rozza, G., Raissi, M., Piccialli, F.: Scientific machine learning through physics-informed neural networks: Where we are and what’s next. *J. Sci. Comput.* **92**(3), 88 (2022) <https://doi.org/10.1007/s10915-022-01939-z>
- [70] Krishnapriyan, A., Gholami, A., Zhe, S., Kirby, R., Mahoney, M.W.: Characterizing possible failure modes in physics-informed neural networks. *Adv. Neural Inf. Process Syst.* **34**, 26548–26560 (2021)
- [71] Bajaj, C., McLennan, L., Andeen, T., Roy, A.: Recipes for when physics fails: recovering robust learning of physics informed neural networks. *Mach. Learn. Sci. Technol.* **4**(1), 015013 (2023) <https://doi.org/10.1088/2632-2153/acb416>
- [72] Qin, S.M., Li, M., Xu, T., Dong, S.Q.: A-wpinn algorithm for the data-driven vector-soliton solutions and parameter discovery of general coupled nonlinear equations. *Physica D* **443**, 133562 (2023) <https://doi.org/10.1016/j.physd.2022.133562>
- [73] Wen, X.K., Jiang, J.H., Liu, W., Dai, C.Q.: Abundant vector soliton prediction and model parameter discovery of the coupled mixed derivative nonlinear schrödinger equation. *Nonlinear Dyn.* **111**(14), 13343–13355 (2023) <https://doi.org/10.1007/s11071-023-08531-6>
- [74] Qiu, W.X., Si, Z.Z., Mou, D.S., Dai, C.Q., Li, J.T., Liu, W.: Data-driven vector degenerate and nondegenerate solitons of coupled nonlocal nonlinear schrödinger equation via improved pinn algorithm. *Nonlinear Dyn.*, 1–14 (2024) <https://doi.org/10.1007/s11071-024-09648-y>
- [75] Pu, J., Peng, W., Chen, Y.: The data-driven localized wave solutions of the derivative nonlinear schrödinger equation by using improved pinn approach. *Wave*



Motion **107**, 102823 (2021) <https://doi.org/10.1016/j.wavemoti.2021.102823>

- [76] Peng, X., Zhao, Y.W., Lü, X.: Data-driven solitons and parameter discovery to the  $(2+1)$ -dimensional nls in optical fiber communications. *Nonlinear Dyn.* **112**(2), 1291–1306 (2024) <https://doi.org/10.1007/s11071-023-09083-5>
- [77] Zhou, H., Pu, J., Chen, Y.: Data-driven forward-inverse problems for the variable coefficients hirota equation using deep learning method. *Nonlinear Dyn.* **111**(16), 14667–14693 (2023) <https://doi.org/10.1007/s11071-023-08641-1>
- [78] Jagtap, A.D., Kawaguchi, K., Em Karniadakis, G.: Locally adaptive activation functions with slope recovery for deep and physics-informed neural networks. *Proc. R. Soc.* **476**(2239), 20200334 (2021) <https://doi.org/10.1098/rspa.2020.0334>
- [79] Lu, L., Meng, X., Mao, Z., Karniadakis, G.E.: Deepxde: A deep learning library for solving differential equations. *SIAM Rev.* **63**(1), 208–228 (2020) <https://doi.org/10.1137/19M1274067>
- [80] Sharma, S., Sharma, S., Athaiya, A.: Activation functions in neural networks. *Towards Data Sci.* **6**(12), 310–316 (2017)
- [81] Rudy, S.H., Brunton, S.L., Proctor, J.L., Kutz, J.N.: Data-driven discovery of partial differential equations. *Sci. Adv.* **3**(4), 1602614 (2017) <https://doi.org/10.1126/sciadv.1602614>
- [82] Kingma, D.P.: Adam: A method for stochastic optimization. arXiv preprint arXiv:1412.6980 (2014)
- [83] Liu, D.C., Nocedal, J.: On the limited memory bfgs method for large scale optimization. *Math. Program.* **45**(1), 503–528 (1989) <https://doi.org/10.1007/BF01589116>
- [84] Stein, M.: Large sample properties of simulations using latin hypercube sampling. *Technometrics* **29**(2), 143–151 (10.1080/00401706.1987.10488205)